# PROCESS EVALUATION AND CHARACTERIZATION OF TUNGSTEN NITRIDE AS A DIFFUSION BARRIER FOR COPPER INTERCONNECT TECHNOLOGY

Bradley Mitsuharu Ekstrom, B. A., M. S.

Dissertation Prepared for the Degree of

DOCTOR OF PHILOSOPHY

UNIVERSITY OF NORTH TEXAS

August 2005

APPROVED:

Jeffry A. Kelber, Major Professor
Oliver Chyan, Committee Member
Paul R. Jones, Committee Member
Michael Richmond, Committee Member
Ajay Jain, Committee Member
Ruthanne D. Thomas, Chair of the Department of Chemistry
Sandra L. Terrell, Dean of the Robert B. Toulouse School of Graduate Studies

Ekstrom, Bradley Mitsuharu, Process Evaluation and Characterization of Tungsten Nitride as a Diffusion Barrier for Copper Interconnect Technology. Doctor of Philosophy (Analytical Chemistry), August 2005, 84 pp., 5 tables, 27 illustrations, 99 titles.

The integration of copper (Cu) and dielectric materials has been outlined in the International Technology Roadmap for Semiconductors (ITRS) as a critical goal for future microelectronic devices. A necessity toward achieving this goal is the development of diffusion barriers that resolve the Cu and dielectric incompatibility. The focus of this research examines the potential use of tungsten nitride as a diffusion barrier by characterizing the interfacial properties with Cu and evaluating its process capability for industrial use.

Tungsten nitride ($\beta$–$W_2N$) development has been carried out using a plasma enhanced chemical vapor deposition (PECVD) technique that utilizes tungsten hexafluoride ($WF_6$), nitrogen ($N_2$), hydrogen ($H_2$), and argon (Ar). Two design of experiments (DOE) were performed to optimize the process with respect to film stoichiometry, resistivity and uniformity across a 200 mm diameter Si wafer. Auger depth profiling showed a 2:1 W:N ratio. X-ray diffraction (XRD) showed a broad peak centered on the $\beta$–$W_2N$ phase. Film resistivity was 270 $\mu$ohm-cm and film uniformity < 3 %. The step coverage (film thickness variance) across a structured etched dielectric ($SiO_2$, 0.35 $\mu$m, 3:1 aspect ratio) was > 44 %. Secondary ion mass spectroscopy (SIMS) measurements showed good barrier performance for $W_2N$ between Cu and $SiO_2$ with no intermixing of the Cu and silicon when annealed to 390 $^oC$ for 3 hours.

Cu nucleation behavior and thermal stability on clean and nitrided tungsten foil ($W_xN$ = $\delta$–WN and $\beta$–$W_2N$ phases) have been characterized by Auger electron spectroscopy (AES) and thermal desorption spectroscopy (TDS) under controlled ultra high vacuum (UHV) conditions. At room temperature, the Auger intensity ratio vs. time plots demonstrates layer by layer Cu

growth for the clean tungsten (W) surface and three-dimensional nucleation for the nitride overlayer. Auger intensity ratio vs. temperature measurements for the Cu/W system indicates a stable interface up to 1000 K. For the Cu /$W_xN$/W system, initial Cu diffusion into the nitride overlayer is observed at 550 K.

## ACKNOWLEDGMENTS

Financial support for this research was provided by the Semiconductor Research Corporation (SRC) through the Center for Advanced Interconnect Science and Technology (CAIST) and is gratefully acknowledged. Secondary ion mass spectroscopy, X-Ray diffraction (XRD), scanning electron microscopy (SEM) and other thin film analysis techniques were provided by Advanced Products Research and Development Laboratories (APRDL), Motorola, Semiconductor Products Sector, Austin, Texas and is gratefully acknowledged.

TABLE OF CONTENTS

Page

LIST OF TABLES

Page

LIST OF ILLUSTRATIONS

Page

# CHAPTER 1

## INTRODUCTION

The main driver and sustainer for growth of the semiconductor industry has been the reduction or decrease in device dimensions for improved functionality at a reduced cost (1). Traditional scaling, however, is beginning to show the fundamental limits of the materials (i.e. Al, W) used as the building blocks for integrated circuit fabrication processes the past 30 years. New materials that offer better electrical performance such as Cu are being examined to replace or augment the existing materials to further extend the device scaling approach.

With the introduction of new materials, new and challenging process/integration issues result. The integration of Cu as an interconnect material in multi-level metallization architectures poses severe compatibility problems with $SiO_2$, a commonly used interlayer dielectric, or with low dielectric constant polymers that are being explored for interlayer dielectric applications. Cu does not bond or adhere well to $SiO_2$/polymer surfaces. Poor bonding can lead to unstable interfaces when subjected to thermal and mechanical stress. When an electrical bias is applied at elevated operating temperatures, Cu easily diffuses or migrates through $SiO_2$. This migration can lead to short-circuiting of the transistor, resulting in chip malfunction. It is therefore critical to understand the behavior of Cu with various diffusion barriers/adhesion layers at the metal dielectric

interface in order to properly integrate the high electrical performance of copper toward the production of advanced integrated circuits.

The research presented in this dissertation focuses on the process evaluation and development of tungsten nitride as a diffusion barrier/adhesion layer between copper and silicon oxide. These studies include:

(1) Industrial development and characterization of plasma enhanced chemical vapor deposited (PECVD) tungsten nitride ($\beta$–$W_2N$) films on silicon oxide ($SiO_2$).

(2) Fundamental wetting and thermal stability properties of Cu on tungsten (W) and nitrided tungsten film ($W_xN$ = partial phases consisting of $\delta$–WN and $\beta$–$W_2N$).

Tungsten Nitride ($W_2N$) development was carried out at Advanced Products Research and Development Laboratory, Motorola, (now Freescale) Austin, Texas, using a commercial cluster tool in an industrial clean room environment (particles < 0.01 microns). Surface analytical techniques such as auger depth profiling, X-Ray diffraction (XRD), scanning electron microscopy (SEM), and other techniques where used to characterize the $W_2N$ films ex-situ. Fundamental Cu/barrier properties were characterized under ultra high vacuum (UHV) using Auger electron spectroscopy and thermal desorption spectroscopy (TDS) at the University of North Texas, Denton, Texas.

This dissertation consists of four chapters. Chapter 1 examines the advantages of copper integration with respect to electromigration and RC delay and the use and requirements of diffusion barriers/adhesion layers to resolve Cu integration problems.

Chapter 2 explains the methodology and instrumentation, including the deposition methods used to deposit barriers and the techniques for characterizing barrier performance. Chapter 3 covers the industrial development and characterization of tungsten nitride as a diffusion barrier/adhesion layer with copper. Chapter 4 investigates Cu wetting and thermal stability on W and $W_xN$ films.

## 1.1. Why the Move to Cu?

Aluminum has been the most widely used material for backend interconnections in a semiconductor device. As device dimension continue to shrink, three negative factors exist that limit the use of Al and favor the choice of Cu. The first pertains to interconnect failures associated with electromigration (2). Electromigration is the transport of lattice atoms in the direction of electron flow in the conductor, due to momentum transfer from the electrons to the lattice atom. At large current densities and at higher temperatures, the effect can be very pronounced, resulting in void formation at one end of the conductor and material accumulation at the other. This produces opens and shorts in the electrical circuit. The enhanced mobility of atoms is caused by the direct influence of the electric field on the ionized atoms and the collision of electrons with atoms, leading to a momentum transfer (called electron-wind effect) and atom movement. Where grain-boundary contribution to atomic diffusion is neglected, the atomic flux due to electromigration in a single crystal or large-grained crystal is defined as:

$$J_{atoms} = \frac{NDZ^*qj}{\sigma kT} \qquad (1.1)$$

where N is the atomic density, D atomic diffusivity, Z*q the effective charge on the moving ion, q the electron charge, j the current density, σ the electrical conductivity, k the Boltzmann's constant, and T temperature in degrees K. In table 1.1 the electromigration parameters for Al, Ag, Au, and Cu (calculated as bulk large-grained metals) are compared. ρ is the electrical resistivity, $D_o$ a constant for a given diffusion system and Q the activation energy for electromigration to occur. When applying the table values -Z*, ρ, D to equation 1.1 at 100 $^oC$, Al has a higher value for atomic flux due to electromigration among the four metals (see far right column table 1.1) (2,3). Al also has lower activation energy (Q) for electromigration to occur. In contrast, Cu has a lower value for atomic flux due to electromigration and the highest activation energy for

Table 1.1. Electromigration Parameters of Bulk Materials

| Metal | -Z* | ρ (μΩ-cm) | $D_o$ ($cm^2/s$) | Q(eV) | D ($cm^2/s$) at 100$^o$C | Z*ρD (μΩ-$cm^3/s$) 100$^o$C |
|---|---|---|---|---|---|---|
| Ag | 9.4-23.4 | 1.59 | 1.89 | 2.01 | $1.1x10^{-26}$ | $2.84\text{-}7.07 \times 10^{-25}$ |
| Al | 6.5-16.4 | 2.65 | 1.71 | 1.48 | $2.1x10^{-20}$ | $3.62\text{-}9.12 \times 10^{-19}$ |
| Au | 5.9-7.4 | 2.35 | 0.67 | 1.96 | $2.2x10^{-27}$ | $3.05\text{-}3.83 \times 10^{-26}$ |
| Cu | 3.7-4.3 | 1.67 | 0.78 | 2.19 | $2.1x10^{-30}$ | $1.3\text{-}1.5 \times 10^{-29}$ |

electromigration to occur among the four metals.

Another limiting property of Al is its resistivity (4). As shown in table 1.1, the resistivity for pure Al is 2.65 μΩ-cm vs. 1.7 μΩ-cm for Cu. In practice, Al alloys, rather than pure Al, are used as an interconnect metal (5). To improve electromigration resistance and minimize reactivity with silicon or silicide contact material, Al is alloyed with Cu and Si, which increases resistivity to 3 to 3.5 μΩ-cm. Tungsten, commonly used for vertical interconnects (vias), has a resistivity of 5.65 μΩ-cm. The importance of the

resistivity parameter regarding the choice of metals for backend interconnections in a semiconductor device is due to the interconnect delay or RC time constant.

By reducing the channel length under the gate of a basic metal oxide semiconductor field-effect transistor (MOSFET), the carrier transient time (for a given applied voltage) across the channel or *intrinsic gate delay* decreases, resulting in a faster device. Signal propagation to and from the transistors must occur through the interconnections, which are the basic current carriers. These interconnects are also capacitatively coupled to each other, separated by insulating dielectrics. The effective total resistance of the interconnection and capacitance associated with the dielectric is called the RC time constant or *interconnect delay* defined as:

$$RC = \frac{\rho \ L^2 \ \varepsilon_{ILD}}{t_M \ t_{ILD}} \tag{1.2}$$

where $\rho$, $t_M$, L, $\varepsilon_{ILD}$, and $t_{ILD}$ are the resistivity, thickness, and length of the interconnection and interlayer dielectric (ILD) permittivity and thickness, respectively. The effective measure of device performance or total circuit delay is a composite of the intrinsic device delay and the interconnection delay (RC time constant). Numerous authors have demonstrated that as feature sizes (channel lengths) decrease below 0.5 μm, the interconnection delay contribution dominates the total effective circuit delay (see figure 1.1) (6,7,8) becoming the performance limiter for circuits. According to equation 1.2, for a given $t_M$ and $t_{ILD}$, RC will depend on $\rho$, L, and $\varepsilon_{ILD}$. With the dependence on $\rho$ and the dominant contribution of RC as device dimensions shrink, it is clear that in order

to improve device speeds (lower total circuit delay) the lower resistivity properties of Cu must be investigated to replace Al and W as an interconnect material.

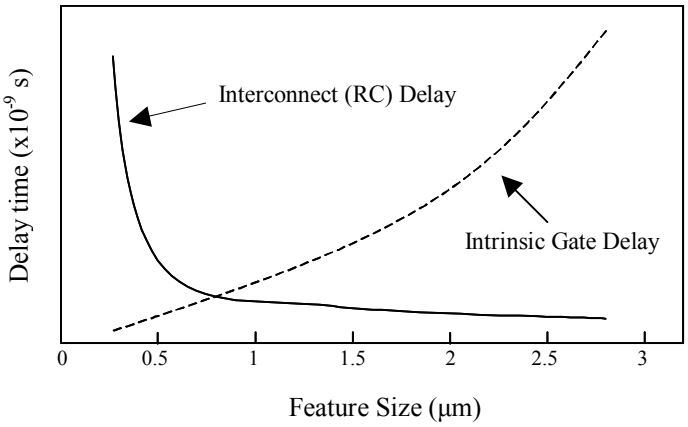


Figure 1.1. Interconnect (RC) delay and intrinsic gate delay as a function of feature size (used with permission from the Materials Research Society, reference 8).

Another benefit of using Cu is that it can actually lead to lower manufacturing costs compared to Al. Because Cu is difficult to etch, a new strategy called "damascene" or "inlaid" patterning was developed to form the interconnect lines (9). The damascene

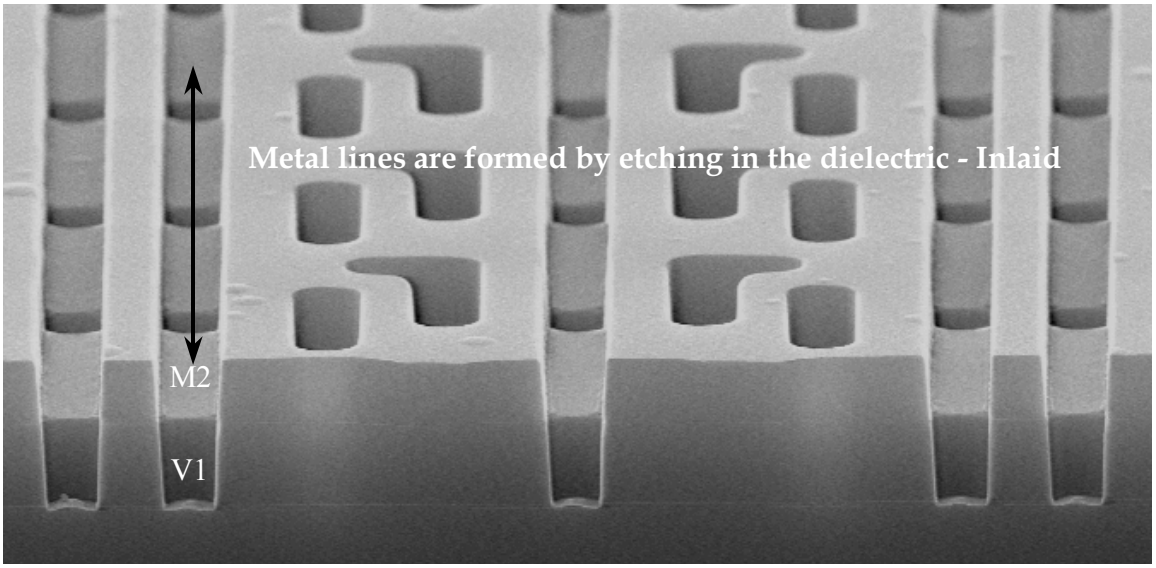


Figure 1.2. Scanning electron microscopy (SEM) image of a dielectric cross section after etching grooves that will form inlaid metal lines and via connections.

process involves etching a blanket dielectric layer in the form of an interconnecting pattern (see figure 1.2) of trenches and vias that are then filled with Cu (the interconnect metal). This approach requires 20-30% fewer steps than traditional subtractive patterning: aluminum etch, tungsten via fill, dielectric and tungsten chemical mechanical polishing (CMP) steps (10).

To summarize, Cu is more favorable than Al as an interconnect material in three ways. Regarding electromigration parameters, Cu in theory demonstrates better electromigration resistance than Al leading to a lower probability of opens and shorts in an electrical circuit. The resistivity of Cu is lower than Al and Al-alloys, effectively reducing the RC time constant or interconnect delay resulting in faster device performance. With the implementation of Cu, a new manufacturing approach called "damascene" is required. This approach eliminates 20-30% of the fabrication steps used in traditional methods, thus reducing manufacturing costs.

## 1.2. Cu Integration Roadblocks

Historically, Cu has not been considered for application in silicon integrated circuits because of its ability to rapidly diffuse in silicon and degrade the semiconductor devices it would be used to connect. In the past, fabs (fabrication facilities) attempting Cu integration programs have lost thousands of product test wafers due to the adverse effects of small amounts of Cu can have on the electrical properties of Si. A possible mechanism for this behavior is that copper appears to have acceptor levels in the middle of the silicon band gap at 0.24, 0.37, and 0.52 eV with respect to the valence edge, and

effectively acts as a recombination-generation center for the charge carriers (11). It has been reported that the silicide compound $Cu_3Si$ forms at a Cu/Si interface at temperatures less than 200 $^{o}$C (12). This temperature is unacceptable for Cu integration requirements where post-metal process temperatures in current integrated circuit manufacturing reach up to 390 $^{o}$C. To avoid the excursionary behavior of the Cu/Si interface for front-end applications (where Cu interfaces with the Si transistor contact metal that form the source, drain and gate polysilicon), Cu has been restricted to the back-end. Here the Cu interconnect is isolated from the silicon substrate by use of a dielectric. The Si transistor

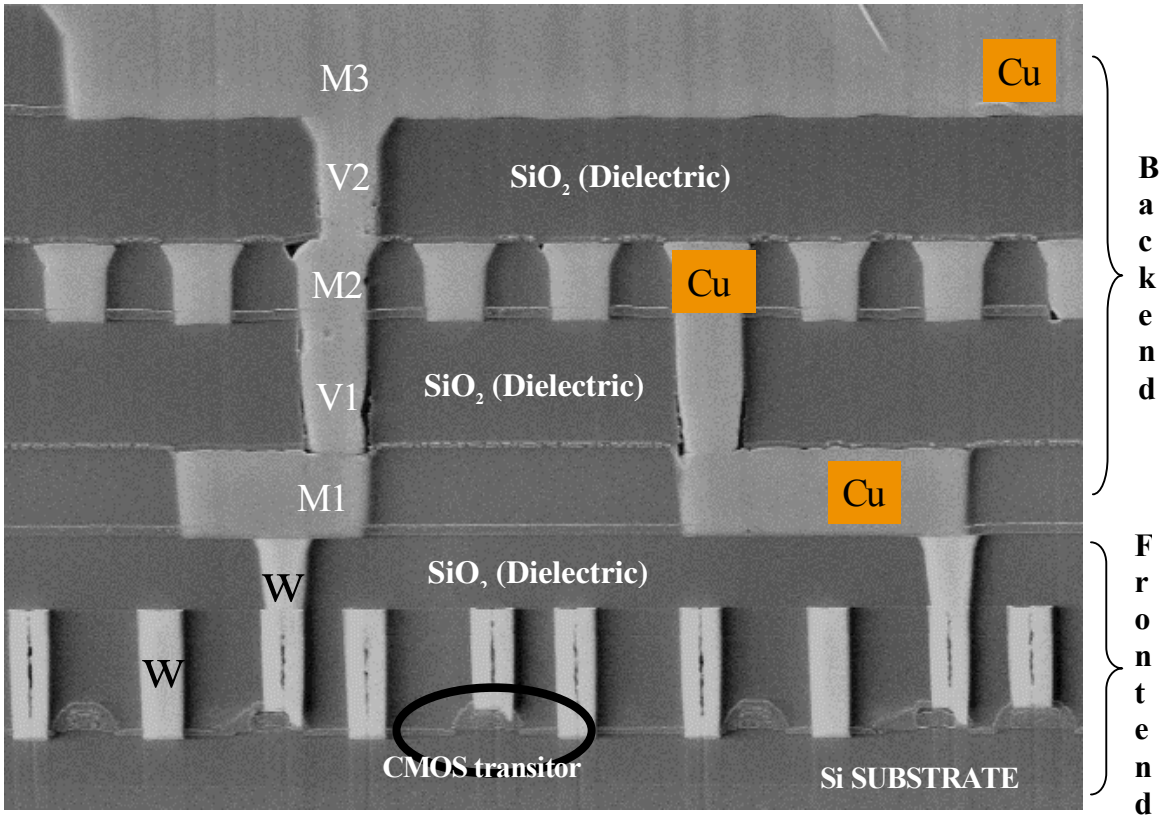


Figure 1.3. Integrated circuit cross section with copper as the interconnect metal, instead of aluminum.

contact is interfaced with tungsten and cobalt silicide ($W/CoSi_2/Si$). The Cu interfaces with the tungsten plug at the first metal layer where the term "backend" processing begins and front-end ends (see figure 1.3). In the backend, Cu would be surrounded by a dielectric or insulating material commonly silicon dioxide ($SiO_2$). As with Si, compatibility issues exist between Cu and $SiO_2$.

In microelectronic manufacturing, the lack of adhesion between two materials can result in material de-bonding degrading the integrated circuit. Copper does not bond well to $SiO_2$. Adhesion between two materials can occur due to a physical bonding attributed to van der Waal's forces or chemical bonding across the interface between the two materials. It is the chemical bonding that is strong and provides stability or adhesion when subjected to forces of a thermal or mechanical nature (13). Shown in table 1.2 are heats of formation for copper and silicon compounds (14). Note that the heats of formations for Cu compounds that would normally be formed at Cu/dielectric interfaces (i.e. $SiO_2$, SiON, SiOF) are much lower than heats of formations for Si compounds. Thus, copper will not reduce $SiO_2$ and is not expected to adhere well to $SiO_2$ surfaces. It has also been demonstrated by McBrayer and co-workers (15) that Cu diffuses into $SiO_2$

Table 1.2. Heats of formation (kcal per nonmetal atom) at 298 $^oC$.

| **Element** | **Oxides** | **Nitrides** | **Fluorides** |
|---|---|---|---|
| Cu | 37 to 40 | -18 | 60 |
| Si | 108 | 44 | 96 |

at 400 $^{o}$C. If used in backend integrated circuit processing, at elevated temperatures Cu will compromise the surrounding dielectric/insulator ($SiO_2$) resulting in leakage currents and cross talk between the interconnects (transistor malfunction). A method to alleviate the Cu/dielectric (and possibly Cu/Si) incompatibility is to introduce a new interfacial material that acts as both an adhesion promoter and diffusion barrier.

### 1.3. Requirements for Cu Adhesion Promoters and Diffusion Barriers

The terms adhesion promoter and diffusion barrier are often used interchangeably in the microelectronics industry. An ideal adhesion promoter provides strong chemical bonding at an interface via a self-limiting reaction. One example of a self limiting reaction is the behavior of aluminum metal forming a passivating oxide when exposed to air (16). The adhesion promoter must also effectively minimize the total free energy of the metal/dielectric interface or prevent the initial interfacial bonding reaction from continuously occurring over time. If the adhesion reaction continuously occurs or does not reach equilibrium before the adhesion material is consumed, the metal/dielectric interface is compromised. Therefore, the adhesion promoter material must also act as a diffusion barrier.

Even though the important requirements for Cu diffusion barriers are good adhesion and diffusion resistance in microelectronics, there are other unique requirements. These include low resistivity, high conformality, and low stress. The following subsections will provide a more in depth explanation of the various adhesion and diffusion resistance barrier requirements in terms of microelectronic fabrication.

### 1.3.1. Strong Adhesion

Adhesion of deposited films in Ultra Large Scale Integration (ULSI) processing must be strong both *as deposited*, and after subsequent processing (ie thermal cycling). If films lift from the substrate device failure can result, and thus poor adhesion represents a potential reliability problem. Two well-known methods to characterize adhesion is the scratch tape peel test and a fracture mechanics technique called four point bending (not covered). The interfacial wetting can be characterized by Auger electron spectroscopy.

### 1.3.2. Minimization of Chemical Interdiffusion and Limit Chemical Interactions

In microelectronics, the electrical contacts to and from the millions of transistors are constructed through multilayer film structures. Combinations of materials are bound to each other by interfaces. Some individual films contain structural defects, such as grain boundaries and dislocations. Rarely is this assembly in thermodynamic equilibrium. Atomic migration occurs to establish equilibrium by lowering the total free energy of the assembly. The driving force for the atomic motion is the gradient of the chemical potential of the atoms in the assembly. A gradient in chemical potential can originate from a concentration gradient, a negative free energy of reaction, an electric field, and a strain gradient (17). For the process evaluation stages of diffusion barrier development, the characterization of concentration gradients and negative free energy of reaction behavior are critical.

The efficiency of a diffusion barrier material is determined by how well it diminishes mass transport across the interface. This in turn depends on the microstructure of the film. The general ordering of diffusion rate or diffusivity as a

function of microstructure type is as follows: grain boundaries (polycrystalline films) > amorphous films (no periodic lattice) > single crystal films (lattice diffusion) (18,19). Ideally, single crystal films would be the preferred microstructure for diffusion barriers. But it is highly impractical and costly to implement single crystal films for integrated circuit manufacturing. Therefore, the next best choice is amorphous films. Amorphous films have only short-range atomic order. Compound units in amorphous films are joined randomly and are therefore devoid of microstructure (no grain boundaries). Therefore, amorphous diffusion barriers are preferred because grain boundary diffusion is

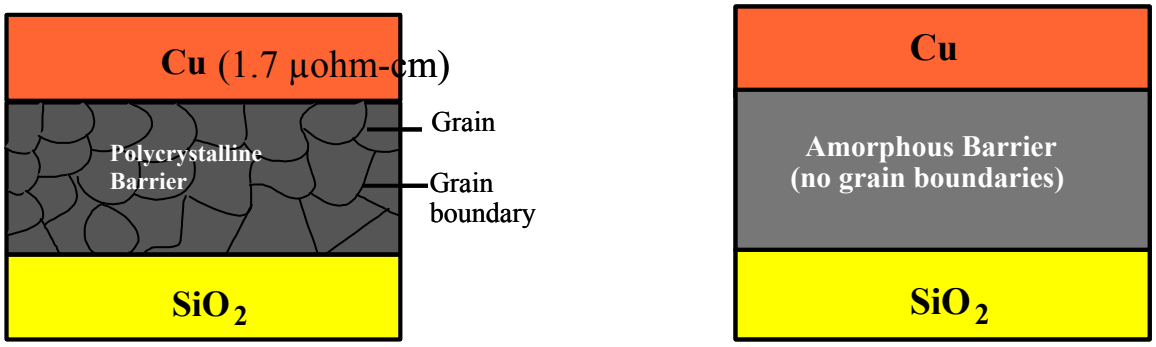


Figure 1.4. Amorphous films are devoid of microstructure minimizing grain boundary diffusion pathways and are thus, ideal diffusion barriers.

minimized (see figure 1.4). One way to achieve amorphous films is through chemical vapor deposition (CVD) (see Chapter 2, section 2.11). Two techniques to measure film microstructure are X-ray diffraction (XRD) and transmission electron microscopy (TEM).

Introducing barrier layers can reduce the total free energy of a thin film system. A multilayer thin film system is in stable chemical equilibrium as long as any change in temperature, concentration, or pressure does not decrease the total free energy of the

system. If the total free energy is decreased, a spontaneous chemical reaction may occur. The thermodynamic criterion for a chemical reaction to take place at a given temperature is a negative Gibbs free energy of change ($\Delta G$) for the reaction $\Delta G = \Delta H - T\Delta S$, where $\Delta H$ is the change in enthalpy and $\Delta S$ is the change in entropy (16, 17). Normally, the contribution from $\Delta S$ is small and the reaction is mainly determined by $\Delta H$. Thus the main driving force for an interfacial reaction is a difference in chemical free energy. Example: Two thin films A and B in contact with each other have a tendency to react and form a compound AB. Imposing a diffusion barrier C, between A and B minimizes the total free energy of the system compared to A/B. Ideally, diffusion barrier C would establish complete chemical equilibrium in the A/C/B system, but in practice an interfacial reaction with C still occurs. It is important that some interfacial reaction for C occurs between A and B to establish good adhesion, but more important that the reaction is self limiting or reaches equilibrium before the whole amount of C is consumed as to not compromise the layer.

Studying interfacial reactions, thermal stability and material diffusivity can be probed by, using electrical measurements (i.e. Capacitance vs. Voltage plots) and various spectroscopy techniques. Reliability studies of Cu integrated circuits reported by Wong et. al. (20) demonstrated that electrical measurements provide better analysis and sensitivity into material diffusion than spectroscopy measurements. Studies reported in this dissertation focus on the use of surface spectroscopic techniques in order to probe the effects of barrier chemical composition (W vs. $W_xN$) on Cu/Barrier interactions. For interfacial reaction and thermal stability studies Auger electron spectroscopy (AES) and

thermal desorption spectroscopy (TDS) have been employed. Secondary ion mass spectroscopy (SIMS) has been used to measure material intermixing or diffusion barrier resistance. Each of these techniques will be further explained in Chapter 2.

### 1.3.3. Low Resistivity and Low Thickness

In the Cu damascene approach for integrated circuit manufacturing, Cu is used for both via and metal interconnect material. The Cu deposition step deposits Cu for both the vias and metal lines simultaneously (dual-damascene or dual inlaid). Wherever Cu is deposited, a diffusion barrier must be interposed. This results in a diffusion barrier between the lower metal line and the interconnecting via (see figure 1.5). If the diffusion barrier is not of a reasonable resistivity (< 800 μohm-cm) (21), signal processing speed (RC delay) will be affected. Also, the barrier must be thin to further minimize the

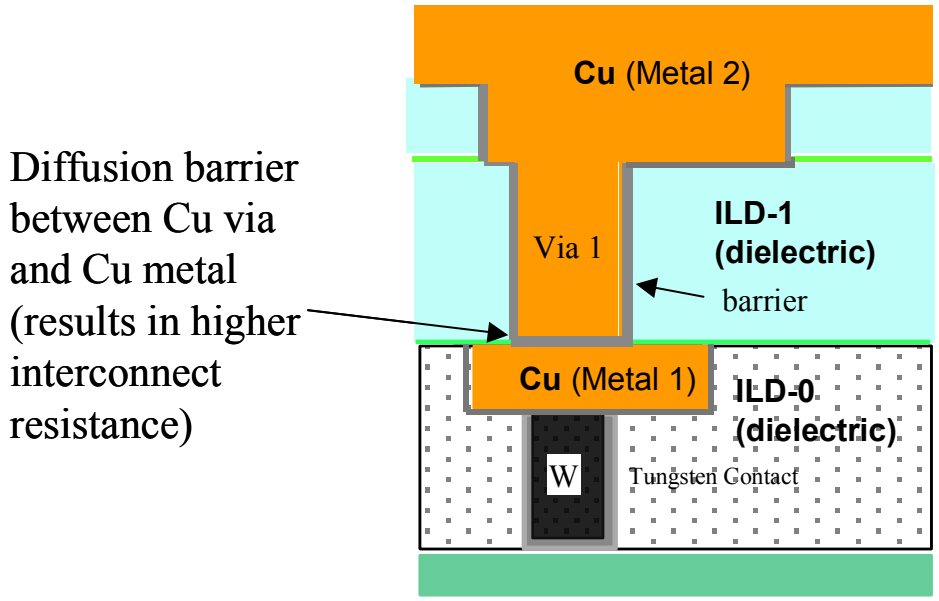


Figure 1.5. Diffusion barrier between Cu via and Cu metal can result in higher interconnect resistance. Therefore the diffusion barrier must have low resistivity and be as thin as possible.

resistance impact on signal processing speed. A technique to evaluate materials resistivity is called four point probe (22). It measures the sheet resistance point by point on non-conductive, semi-conductive or conductive films deposited on a large area i.e. 200 mm diameter Si wafer resulting in a sheet resistance profile. The sheet resistance average and average film thickness measured by Secondary Electron Microscopy (SEM) Cross-sectional thickness measurements are used to determine approximate resistivity. Four point probe and SEM along with resistivity calculations are discussed further in Chapter 2.

### 1.3.4. Good Feature Conformality through Chemical Vapor Deposition (CVD) Processing

Conformality, or step coverage of a thin film refers to its capability to exactly reproduce the surface coverage and is defined as side wall thickness divided by the

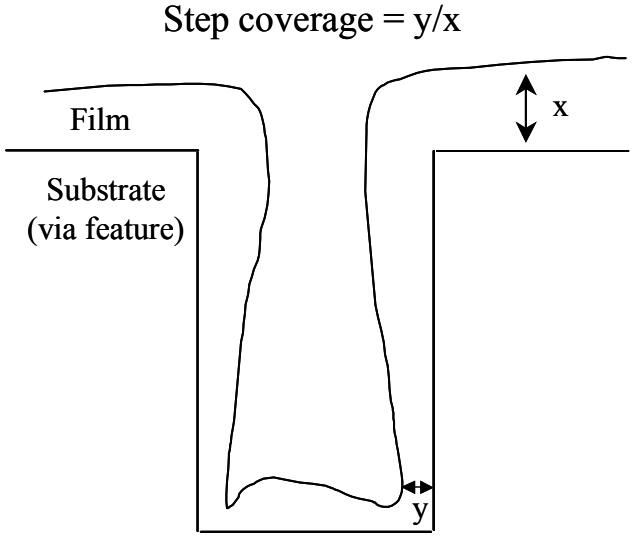


Figure 1.6. Schematic of how step coverage (a measurement of conformality) is measured over a via feature.

thickness of a film on top of the feature (see figure 1.6). Conformality is important because microelectronic processing proceeds by successively depositing and patterning features on thin films. For industrial purposes, ideal step coverage would be 100% so as to limit thickness marginalities that would compromise the conforming layer performance (1). If successive films do not follow the patterns created on the previous layers, voids or improper filling of patterned features such as vias or trenches result. These voids in the electrical design architecture lead to electrical shorts and opens. These voids can also act as cavities for contaminants of subsequent processing (i.e. chemical mechanical polishing slurry) compromising the material design (metal, insulator, semiconductor poisoning) integrity of the integrated circuit (23). Conformality values less than 100% are acceptable as long as these marginalities are limited.

The most widely used techniques for producing films in the microelectronics industry are physical vapor deposition (PVD) (24) and chemical vapor deposition (CVD) (24, 25). In physical vapor deposition, the propagation or flux of deposited material is more directional or "line of sight" and sticks to a surface with little or no surface mobility after arrival (24, 26-28). As device dimensions continue to shrink, the probability of conformally filling device features such as vias (round holes) and trenches becomes more of a challenge (1, 29-32). Films produced with chemical vapor deposition are less sensitive to reduced device dimensions due to the surface mobility of the reactant precursors and the thermal energy applied to the substrate to complete film formation. For a period of time, the reactant precursors migrate across a substrate surface before they either consume the thermal energy and convert into the resulting film or desorb off

(25, 33, 34). The surface mobility of the reactant precursors and formation dependence on temperature leads to more conformal deposited trenches and vias. It is this property that makes CVD the leading technique for the deposition of Cu diffusion barriers to meet the demands of future shrinking device dimensions. In Chapter 2, the CVD technique will be further discussed.

### 1.3.5. High Uniformity

It is critical that diffusion barriers have high uniformity across a large sample area for ULSI applications. The reason is that lithographic imagers are used in microelectronic manufacturing to pattern very small features across the substrate (i.e. 200 mm diameter Si wafer). These imaging tools have limited depths of focus and require that each successive layer is sufficiently uniform (35). A qualitative technique to measure uniformity is tilt scanning electron microscopy (SEM) where imaging of the sample is taken off angle from surface normal giving a semi-three dimensional visual of the surface. Quantitative measurements include determining the sheet resistance percent standard deviation of 49 points across a wafer using four point probe (see section 1.3.3) and performing a root mean square (surface roughness) measurement using Atomic Force Microscopy (AFM). The SEM, four-point probe and AFM techniques are further described in Chapter 2.

### 1.3.6. Low Stress

In Ultra Large Scale Integration (ULSI) applications, thin films under high stress are undesirable due to a number of failure modes. One result of high stress is the

cracking or failure of a brittle material, such as a dielectric on an underlying polysilicon layer (36). A diffusion barrier that "cracks" would easily allow the subsequently deposited interconnect metal to poison the underlying dielectric. Another result of highly stressed films is delamination or poor adhesion. Films under high stress, whether extremes of tensile or compressive stress (see Chapter 2, section 2.8), are more probable to lift off the critical device substrates (37-39). Thus the diffusion barrier/substrate must demonstrate low stress properties in order to be of any significance. In Chapter 2, the technique to measure the stress between a deposited film and substrate is further discussed.

## 1.4. Summary

To summarize, the following requirements and analytical techniques to characterize Cu diffusion barriers are tabulated in table 1.3. The next chapter will focus on describing each analytical technique used to characterize diffusion barrier/adhesion layers. Chemical vapor deposition, the technique deemed ideal for depositing Cu/diffusion barriers/adhesion layers films will also be reviewed. It is necessary to explain these methodologies that are used to obtain critical characterization data presented in chapters 3 and 4.

Table 1.3. Reasons for diffusion barrier/adhesion layer requirements.

| Diffusion barrier/adhesion layer requirements | Reason | Analysis technique to measure properties |
|---|---|---|
| Strong adhesion | Prevents film lifting in multi-level metallization architectures. | Scratch tape peel test, Auger electron spectroscopy (AES), thermal desorption spectroscopy (TDS) |
| Amorphous | To minimize grain boundary diffusion. | X-Ray diffraction (XRD), transmission electron microscopy (TEM) |
| Self limiting/low chemical interaction | To minimize chemical inter-diffusion. | Auger electron spectroscopy (AES), secondary ion mass spectroscopy (SIMS) |
| Low resistivity | To minimize resistance impact between via and metal line in the dual damascene approach. | Four-point probe sheet resistance measurement |
| Low thickness | To minimize resistance impact between via and metal line in the dual damascene approach. | Scanning electron microscopy (SEM) cross section thickness measurement. |
| Good feature conformality or high step coverage through chemical vapor deposition (CVD) | To insure topographical reproducibility.<br>To minimize voiding that lessens the probability of short and opens. | SEM cross sectional measurement of the tightest via feature within the device. |
| High uniformity | To insure uniform film integrity across large areas (low surface roughness) and minimize focus spots issues during lithographic imaging. | Four-point probe electrical testing profile (ie 49 point sheet resistance map across a 200 mm wafer),<br>tilt-SEM,<br>atomic force microscopy (AFM). |
| Low stress | To minimize poor adhesion and cracking. | Wafer curvature (before and after film deposition). |

## 1.5. Chapter References


(1) The International Technology Roadmap For Semiconductors. 1999.

(2) Huntington, H. B. *Diffusion in Solids –Recent Developments*; Nowick, A. S. and Burton, J.J.; Eds.; Academic Press: New York, 1975; p. 303.

(3) Peterson, N. L. *Diffusion in Solids - Recent Developments*; Nowick, A. S. and Burton, J. J.; Eds.; Academic Press: New York, 1975; p. 116.

(4) Murarka, S. P. Proc. *Int. Conf. Adv. Microelectronic Devices and Processing, Tohoku University, Sendai, Japan*. March 3 to 5, 1994, p. 321.

(5) Murarka, Shyam P.; Hymes, Steven W. *Critical Reviews in Solid State and Materials Sciences*. **1995**, *20 (2)*, 87-124.

(6} Sinha, A. K.; Cooper, J. A. Jr.; Levinstein, H. H. *Electron. Dev. Lett*. **1982**, *3*, 90.

(7) Saraswat, K. C.; Mohammadi, F. *IEEE, Trans. Electron. Dev*. **1982**, *29*, 645.

(8) Jeng, S.-P.; Havemann, R. H.; Chang, M.-C. *Mater. Res. Soc. Symp. Proc*. **1994**, *337*, 25.

(9) Singer, P. *Semiconductor International*. **1997**, *20 (8)*, 79.

(10) Singer, P. *Semiconductor International*. **1998**, *21 (6)*, 91-98.

(11) Milnes, A. G. *Deep Impurities in Semiconductors*; John Wiley & Sons: New York, 1973, pp. 1-526.

(12) Stolt, L.; d'Heurle, F.M.; Harper, J.M.E. *Thin Solid Films*. **1991**, *200*, 147.

(13) Muraka, S. P. *Metallization Theory and Practice for VLSI and ULSI*; Butterworth-Heinemann: Boston, MA, 1993; pp. 70-74.

(14) Kubaschewski, O.; Evans, E. L.; Alcock, C. B. *Metallurgical Thermochemistry, 4th ed*.; Pergamon Press: Oxford, New York, 1967; pp. 1-495.

(15) McBrayer, J. D.; Swanson, R. M.; Sigmon, T. W. *Journal of the Electrochemical Society*. **1986**, *133*, 1243.

(16) Ebbing, Darrell D. *General Chemistry 2nd ed.;* Houghton Mifflin: Boston, MA, 1987, p. 790.

(17) Wittmer, M. *Journal of Vacuum Science and Technology A*. **1984**, *2(2)*, 273-280.

(18) Gupta, D.; Tu, K. N.; Asai, K. W. *Phys. Rev. Lett.* **1975**, *35*, 796.

(19) Chen, H.S.; Kimerling, L.C.; Poate, J.M.; Brown, W.L. *Appl. Phys. Lett.* **1978**, *32*, 461.

(20) Wong, S. S.; Cho, J. S.; Kang, H.; Ryu, C. *Mat. Chem. & Phys.* **1995**, *41*, 229-233.

(21) Mori, H.; Imahori, J. Oku, T.; Murakami, M. *AIP Conference Proceedings*, **1998**, *418*, 475-480.

(22) Prometrix Auto RS55/tc manuel, # 04-0187 A, 1994, pp. A1 - A9.

(23) Siviram, S. *Chemical Vapor Deposition: Thermal and Plasma Deposition of Electronic Materials*; Van Nostrand Reinhold: New York, 1995; pp. 35-36.

(24) Muraka, S. P. *Metallization Theory and Practice for VLSI and ULSI*; Butterworth-Heinemann: Boston, MA, 1993; pp. 126-136.

(25) Siviram, S. *Chemical Vapor Deposition: Thermal and Plasma Deposition of Electronic Materials*; Van Nostrand Reinhold: New York, 1995; pp. 1-292.

(26) Nguyen, T.; Charneski, L.; Hsu, S. T. *Journal of the Electrochemical Society.* **1997,** *144 (8)*, 2829-2833.

(27) Vazues, L.; Salvarezza, R. A.; Levy, R. A. *Applied Physical Letters*. **1996**, *68 (9)*, 1285-1287.

(28) Ekerdt, J. G.; Sun, Y. M.; Szabo, A.; Szulczewski, G. J.; White, J. M. *Chemical Review.* **1996**, *96*, 1499-1517.

(29) Singer, P. *Semiconductor International*. February 1996, pp. 89-94.

(30) Siviram, S. *Chemical Vapor Deposition: Thermal and Plasma Deposition of Electronic Materials*; Van Nostrand Reinhold: New York, 1995; pp. 94-133.

(31) Jain, A.; Ekstrom, B.; Adetutu, O. *Conference Proceedings ULSI Materials Research Society*, **1999**, *14*, 305-311.

(32) Kelsey, J.; Goldberg, C.; Nuesca, G.; Peterson, G.; Kaloyeros, A.; Arkles, B. *J. Vac. Sci. Technol. B*. **1999**, *17(3)*, 1101-1104.

(33) Wolf, S.; Tauber, R. N. *Silicon Processing for the VLSI Era, Volume 1 - Process Technology*; Lattice Press: Sunset Beach, CA, 1986; pp. 161-197.

(34) Gates, S. M. *Chemical Review*, **1996**, *96*, 1519-1532.

(35) Siviram, S. *Chemical Vapor Deposition: Thermal and Plasma Deposition of Electronic Materials*; Van Nostrand Reinhold: New York, 1995; pp. 34-35.

(36) Shirley, G. G.; Blish, R. C. *Proceedings of the 25th Annual International Reliability Symposium, IEEE*. **1987**, 73.

(37) Mittal, K. L. *Vacuum Technology and Coating*. **2001**, *2 (12)*, 45-48.

(38) Gray, W. D.; Loboda, M. J. *Solid State Technology*. March 2002, pp. 37-40.

(39) Wolf, S.; Tauber, R. N. *Silicon Processing for the VLSI Era, Volume 1 - Process Technology*; Lattice Press: Sunset Beach, CA, 1986; pp. 114-118.

# CHAPTER 2

# ANALYTICAL METHODS AND CHEMICIAL VAPOR DEPOSITION FOR THE MICORELECTRONICS INDUSTRY

## 2.1. Introduction

This chapter presents numerous analytical techniques used in the microelectronics industry. The goal of this chapter is to provide background for each analytical technique used to examine Cu diffusion barrier/adhesion layer properties (Table 2.1). These

Table 2.1. Properties characterized by analytical technique.

| Analytical Technique | Property Characterized | Chapter applied |
|---|---|---|
| X-Ray diffraction (XRD) | Microstructure | 3 |
| Transmission electron microscopy (TEM) | Microstructure | 3 |
| Scratch tape peel test | Interfacial adhesion (gross reality check) | 3 |
| Auger electron spectroscopy (AES) | Interfacial wetting and inter-diffusion | 3, 4 |
| Secondary ion mass spectroscopy (SIMS) | Inter-diffusion | 3 |
| Four point probe sheet resistance measurement | Sheet resistance | 3 |
| Scanning electron microscopy (SEM) | Sub-micron imaging, thickness measurement, step coverage, surface roughness (gross reality check) | 3 |
| Atomic force microscopy (AFM) | Surface roughness | 3 |
| Wafer curvature | Stress | 3 |
| Thermal desorption spectroscopy (TDS) | Adsorbate-substrate interfacial strength | 4 |

techniques are applied in chapter 3 and 4 to characterize tungsten nitride ($W_xN$) properties, especially diffusion barrier/adhesion layer performance with respect to Copper.

A basic understanding of chemical vapor deposition (CVD) will also be discussed. In chapter 3, the tungsten nitride films were produced with a plasma enhanced chemical vapor deposition (PECVD) reactor. By achieving films with CVD, it is important to discuss the various input parameters (i.e. flow rate, pressure, etc) that can govern thin film properties and how these properties are characterized (1-6).

## 2.2. X-Ray Diffraction (XRD)

The analysis of the angular position and intensity of x-rays diffracted by crystalline material can reveal information on the crystal structure and crystalline phases present in the sample (7-9). X-Ray diffraction occurs when the Bragg requirement is satisfied:

$$n\lambda = 2d\sin\theta \tag{2.1}$$

where $\lambda$ is the x-ray wavelength, d is the interplanar spacing, $\theta$ is the Bragg diffraction angle, and n is the integer giving the order of the diffraction.

## 2.3. Scanning Electron Microscopy (SEM)

Superior to optical microscopy, scanning electron microscopy can provide better magnification (up to 300,000x), resolution (> 10 Å) and depth of focus (2-4 μm) (10-12). A source generates a beam of electrons (the primary electron beam) that is accelerated to energies of 500 eV to 40 KeV, focused to a small diameter, and directed at the surface of a sample in a raster-scan pattern. The electrons striking a surface cause the emission of

electrons and x-rays. Three types of electrons emitted are the low or secondary electrons (0-50 eV), high energy or back-scattered electrons (near or equal to the primary beam energy) and Auger electrons (20 to 1000 eV). Inelastic collisions of the primary beam and the inner shell electrons of the sample atoms produce the low energy or secondary electrons. The back-scattered emitted electrons are those that have suffered elastic conditions with target atoms and thus still possess most of their incident energy. Auger electron processes and analysis will be discussed in section 2.5. The most useful for morphological studies with SEM are the low or secondary electrons. The generated secondary electrons are intensity-modulated on the z-axis of a cathode ray tube (CRT) or detector. An image of the sample surface is produced on the CRT screen by synchronously raster scanning the CRT screen and the electron beam of the SEM. The contrast of the image is dependent on the variations in flux of electrons arriving at the detector. The yield of emitted secondary electrons is dependent on the work function of the material. With oxides, semiconductors and metals all exhibiting different work functions, the SEM technique can readily distinguish these material types through variations in contrast. The resolution of the SEM depends on the sample type, the electron source, focusing optics, and accelerating voltage of the primary beam.

## 2.4. Transmission Electron Microscopy (TEM)

Just as shrinking line widths and vertical feature sizes led to the displacement of optical microscopes by the SEM, other applications for which the SEM had been adequate now require an even higher resolution technique called transmission electron microscopy (TEM). In contrast to SEM, with typical spatial resolutions 20 to 30 Å, TEM

offers 2 Å resolutions or better (13-15). The image in TEM is produced by the differential loss of electrons from an incident beam (60-350 KeV, electron wavelength ~0.04 Å) as it passes through very thin film samples. The sample must be thin enough to transmit the beam, so that essential information caused by differences in the sample thickness, phase composition, crystal structure, and orientation is preserved. In a conventional TEM, the electron beam is focused by a condenser lens, then passes through the sample and is imaged onto a photographic plate or fluorescent screen. TEM is capable of imaging the grains of polycrystalline films and is very useful for measuring grain sizes and structural anomalies in thin films. The contrast in a TEM image differs between crystalline and amorphous materials. In crystalline layers, the materials diffract the incident electron beam. Abrupt changes in thickness, phase structure, or crystallographic orientation cause corresponding changes in contrast, and these crystallographic features can be easily imaged at high resolution. In amorphous regions, contrast is obtained from difference in sample thickness or from difference in chemical or phase composition. TEM images from amorphous materials (eg oxides, nitrides) are thus somewhat easier to interpret than images from crystalline layers.

## 2.5. Auger Electron Spectroscopy (AES) and Depth Profiling

Auger analysis is an analytical tool for investigating elemental and chemical components of the outermost few atomic layers of a material (16-19). The Auger emission process results from the bombardment of a solid by an energetic electron beam (up to 10 KeV). The process is illustrated in Figure 2.1. The energetic electron beam ejects an electron from a K shell of an atom. An electron from the L2 level of the same

atom relaxes into the K shell, emitting a photon in the process. In some cases, the photon escapes the material, but in others it interacts with and causes the ejection of a lower energy electron. In figure 2.1, the lower energy electron would be from the L3 level. Electrons ejected by this mechanism are called Auger electrons. In order to create one Auger electron, three electrons must be involved. In figure 2.1, one electron was from the K level, one from the L2 level and another form the L3 level. This Auger electron is

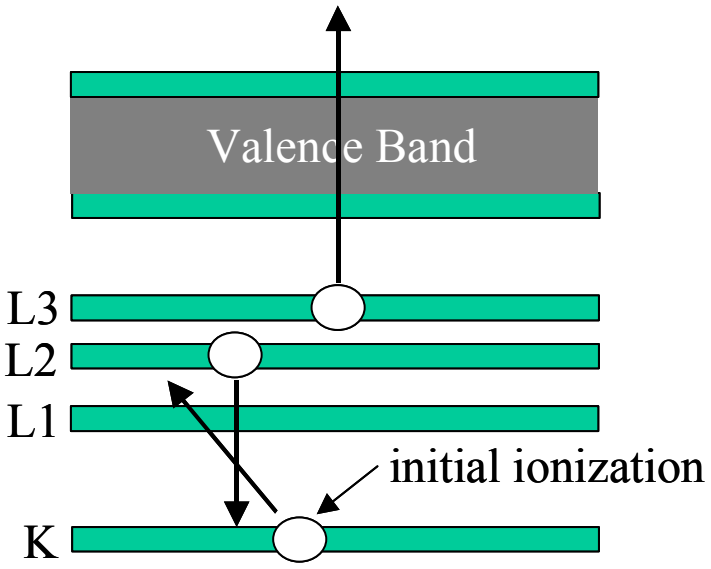


Figure 2.1. Auger electron emission during de-excitation of an atom after initial ionization.

identified as a KLL Auger electron. The energy of the ejected Auger electron ($E_K$) is approximated by: $E_K = E_c - (E_1 + E_2)$ where $E_c$ = the binding energy of the core electron and E1 and E2 = the binding energy of the two higher energy electrons involved in the Auger process. Since the Auger electron energy is dependent on the three energy levels involved and since the binding energies are unique, each element has a characteristic Auger emission (19). Elements with fewer than three electrons (i.e. H and He) cannot

emit Auger electrons and therefore cannot be detected with Auger electron spectroscopy. Auger electron energies are between 10 and 2000 eV (see figure 2.2). The depth from which Auger electrons can escape from the solid without losing a significant percentage of energy can be from 5 to 50 Å. This shallow escape depth is due to the inelastic scattering processes an Auger electron undergoes in a solid and is a consequence of

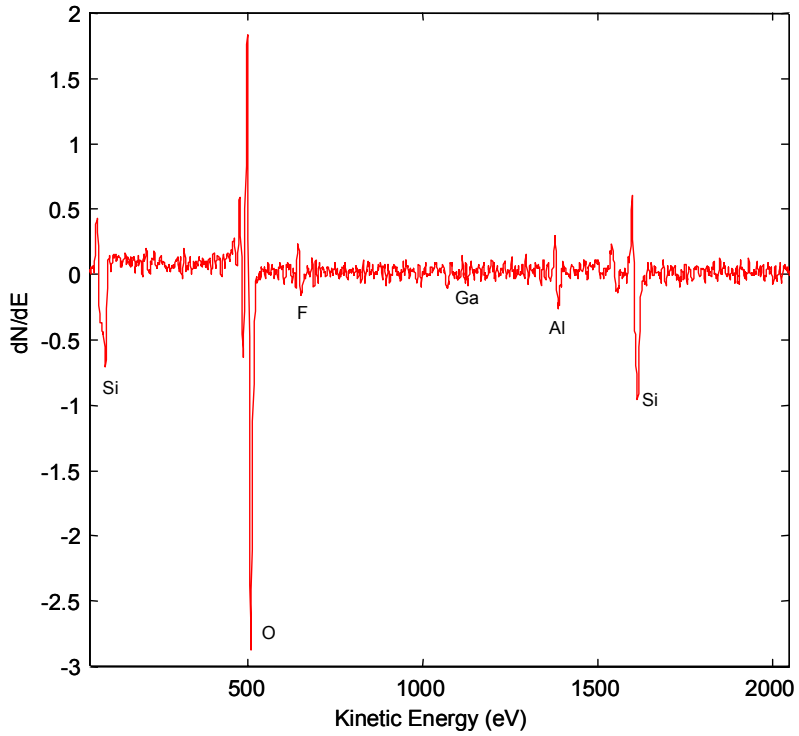


Figure 2.2. Typical Auger spectrum in the derivative mode (dN/dE)

the inelastic mean free path (IMFP). The IMFP is defined as the average distance which a specific energetic electron travels between successive inelastic conditions. For solids, the IMFP is governed by the 'universal curve' where electron energies from 30 to 2000 eV exhibit typical inelastic mean free paths from 5 to 50 atomic layers, respectively (20). Thus, Auger can only provide compositional data about the outermost surface layers of

samples. Typical Auger experimental data yield electron intensity as a function of energy (N vs. eV). But Auger peaks in this way are small due to a rapidly varying secondary electron background and usually displayed as the second derivative of intensity (dN/dE) as a function of eV. The yield of Auger electrons is proportional to the concentration of the elements within the sample volume. Peak to peak (Auger peak heights) intensity measurements in the derivative mode can be used for each element to characterize interactions between elements or compounds i.e. diffusion, inter-mixing, growth-modes and determine possible elemental stoichiometry.

To understand material composition at depths greater than the escape depth of Auger electrons, sputtering or ion bombardment into a sample in conjunction with Auger analysis is used in order to sequentially remove outer layers of the material. The sputtering process is stopped at regular intervals, during which an Auger spectrum is taken. The Auger peak-to-peak intensities can be plotted as a function of sputtering time and thus, a depth profile can be obtained.

## 2.6. Secondary Ion Mass Spectroscopy (SIMS)

In SIMS analysis, material removed from a substrate by ion bombardment is analyzed with a mass spectrometer to generate a sample composition profile or chemical composition vs. depth (21-24). In the SIMS technique, the energetic bombardment (1 - 20 KeV) of a material causes billiard ball-like collisions with atoms of the surface, leading to their ejection from the material (sputtering). During the energy transfer process, a small fraction of the ejected atoms leave as either positively or negatively charged ions. Over 90% of these secondary ions are emitted from the outer two atomic

layers of the sample. The sputter ions are collected by a mass spectrometer (quadrapole type) for mass-to-charge separation and detection. The number of ions collected can also be digitally counted to produce quantitative data on the sample composition. Thus SIMS analyzes the material removed by sputtering from the sample surface.

In order to maximize sensitivity, oxygen atoms are used for sputtering and exciting the electropositive elements (i.e. low ionization potential elements; Na, B, Al, etc) while beams of cesium atoms are employed for producing negative ions from electronegative elements (i.e. high electron affinity elements, C, O, As). The sputtered sample detection limit is sensitive to the beam type. For example, gold doped silicon has a detection limit of ~100 ppm atomic % with an oxygen beam and ~ 0.1 ppm atomic percent with Cs (25).

The sputtering process continuously removes surface atoms. Therefore, the shallow analytical zone defined by the secondary escape depth, is advanced into the sample as a function of sputtering time. By monitoring the secondary ion signals with time, a depth profile can be produced. Sputter rates of 2-5 Å/sec, at data acquisition times of 10 sec, produce typical depth increments (vertical resolution) in the 20-50 Å range. Layers of up to 10,000 Å thick can be depth profiled with SIMS (26). Usually the incident beam is rastered over a small area of the surface to create a crater with a nearly flat bottom. Mass analysis is only performed on the ionic fraction of sputtered material from the center of the crater.

The advantage of SIMS is that it can detect hydrogen and helium whereas other surface science techniques cannot e.g. Auger electron spectroscopy, X-Ray photoelectron

Spectroscopy and Rutherford backscattering. Another advantage is that it can identify elements present in very low concentrations levels ($10^{13}$ to $10^{18}$ atoms/cm$^3$) (27). It is very sensitive to elements with low ionization potential (e.g. Na, K) and high electron affinity (group V and VI elements). It is commonly used to measure doping

Table 2.2. SIMS Detection limits for various dopants in Si.

| Dopant/Contaminant in Si | Minimum Detectable Concentration (atoms/cm$^3$) |
|---|---|
| Arsenic | $5 \times 10^{14}$ |
| Phosphorus | $5 \times 10^{15}$ |
| Boron | $1 \times 10^{13}$ |
| Oxygen | $1 \times 10^{17}$ |
| Hydrogen | $5 \times 10^{18}$ |

level concentrations in electronic materials. Table 2.2 lists SIMS sensitivity limits for various dopants and contaminants in silicon (27).

SIMS has several limitations. The range of beam diameters is typically 1 - 100 μm. Optimal sensitivity is achieved with wider beam diameters (100 μm) (21). Sensitivity relates to the corresponding amount of atoms sputtered. With constant beam density, sensitivity is proportional to beam diameter. For ULSI feature of sub-micron dimensions, the SIMS technique effectiveness is limited. Another limitation is called secondary mass interference. One example is the difficulty of detecting phosphorus in Si when water is present. The Si reacts with hydrogen to form $^{31}SiH^+$, and overlaps with the $^{31}P^+$ mass peak. Other limitations are that the technique is locally destructive, subject to charging especially in dielectric layers and requires standards to obtain quantitative data about the detected constituents.

## 2.7. Atomic Force Microscopy (AFM)

In principle, AFM resembles the record player. It operates by measuring attractive (van der Waals forces) or repulsive forces between a tip and a sample (28, 29). A tip of atomic dimensions can be prepared and brought to a surface in atomic ranges of 0-0.5 nm (0-5 Å) by piezoelectric ceramics that can expand by the application of an external voltage in the range of about 1 volt per angstrom. As the tip is brought to the surface in this way, the tip-surface distance can be stabilized by a force that is equal and opposite to the force operating between the tip and the surface and is usually done by using a spring with a suitable spring constant. The force on the tip, attractive or repulsive, as it approaches the surface can be measured with the sensitivity of $10^{-9}$ Newtons. In repulsive "contact" mode, a tip at the end of a leaf spring or "cantilever" lightly touches a sample. As a raster-scan drags the tip over the sample, a form of detection apparatus (typically a laser beam) measures the vertical deflection of the cantilever, which indicates the local sample height. Thus, in contact mode the AFM measures hard-sphere repulsion forces between the tip and sample. In non-contact mode, the AFM derives topographic images from measurements of attractive forces; the tip does not touch the sample. AFMs can achieve resolutions up to the atomic level (30). And unlike electron microscopes, can image samples in air and liquids and measure non-conductive samples without charging issues. AFM is useful in the Semiconductor industry to measure the surface roughness of thin films. Surface roughness measurements can provide an average distance between the lowest point and highest point across a film surface area. This is useful to understand a film thickness limit of

conformality or consistent film coverage across a given area by a particular deposition method.

## 2.8. Wafer Curvature: Stress Measurement

Most films are in a state of internal stress. Stress may be compressive or tensile. Compressively stressed films have a tendency to expand parallel to the substrate surface and causes convex bending of the substrate (negative value). Films that exhibit tensile stress tend to contract parallel to the substrate and causes concave bending of the substrate (positive value) (31).

A technique to measure the stress impact imposed by a deposited film on a substrate (wafer) is to measure the substrates change in radius of curvature. The stress ($\sigma$) in the film is calculated from the radius of curvature of the substrate using the following equation (32):

$$\sigma = \frac{E\, h^2}{(1-\nu)\, 6\, R\, t} \tag{2.2}$$

where $E/(1-\nu)$ is the biaxial elastic modulus of the substrate ($1.805 \times 10^{11}$ for (100) silicon wafers, $h$ is the substrate thickness (m), $t$ is the film thickness (m), R is the substrate radius of curvature (m) and $\sigma$ is the average film stress (Pa). The substrate radius of curvature is defined as $R = (R_1R_2)/(R_1-R_2)$ where $R_1$ is the average radius of the un-deposited substrate and $R_2$ is the new radius of the deformed substrate after the film is deposited. To calculate the stress, the substrate radius must be measured before and after film deposition.

## 2.9. Four Point Probe Sheet Resistance Measurement

The four-point probe is used to obtain the sheet resistance ($R_s$) of thin layers ie metals, semiconductors that help determine the resistivity ($\rho$) of large-volume samples, ie 200 mm wafer (33). Resistivity ($\rho$) is a measure of the inability of a layer to support the conduction of electrical carriers (34). In a metal layer, these carriers are electrons. For semiconductor layers, these carriers can be electrons (n-type material) or holes (p-type material). Resistivity is a bulk property of a material and its units are ohm-centimeters ($\Omega$-cm). It is a function of the carrier concentration, n, and the carrier mobility, $\mu$, as expressed in the equation:

$$\rho = \frac{1}{ne\mu} \tag{2.3}$$

where e, is the electronic charge. When characterizing thin layers, it is useful to introduce the concept of resistance per unit area, or sheet resistance. The sheet resistance ($R_s$), of a homogeneous layer is represented by:

$$R_s = \frac{\rho}{t} \tag{2.4}$$

where t is the thickness of the layer. The total resistance R is represented by the product of $R_s$ and the (length/width) of the material:

$$R = \frac{V}{I} = R_s \frac{\text{length}}{\text{width}} \tag{2.5}$$

Four point probe assemblies can be either of a linear or square array arrangement. The four-point probe used to measure sheet resistance and obtain resistivity of the tungsten nitride films in chapter 3 had a linear array arrangement. Typical linear array probe spacings range from 0.64 to 1.6 mm. Probe force, tip radius and probe material must be selected with respect to the resistivity, hardness and thickness of the layer measured. The sheet resistance $R_s$ is obtained by introducing a current I through two pins

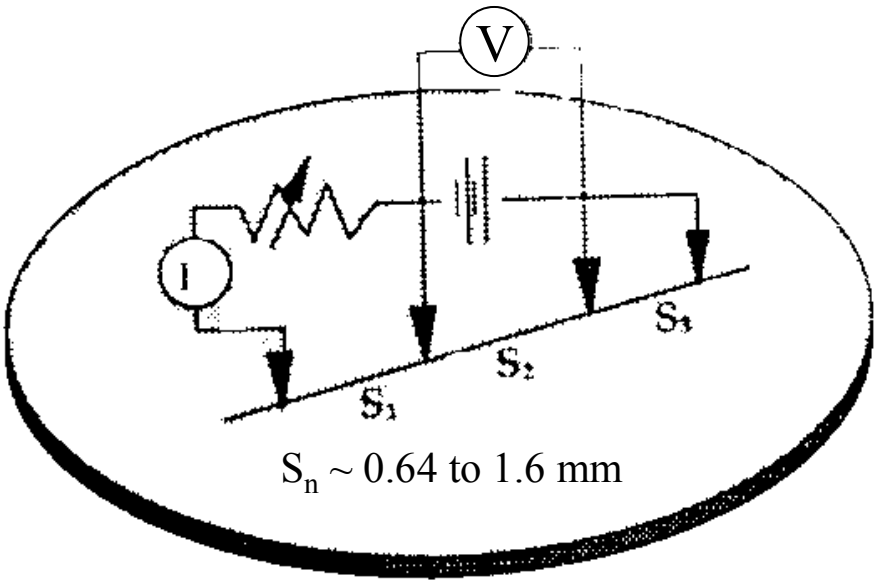


Figure 2.3. A four point probe linear array.

and determining the voltage drop V across the two remaining pins. In the linear array arrangement, the two out pins carry current and the inner two pins measure the resulting voltage (see figure 2.3). With a probe tip spacing equal (S1=S2=S3) and the sample area large (i.e. 200 mm wafer) compared to the probe tip spacing the following equation applies to determine $R_s$ with a four point probe linear arrangement:

$$R_s = \frac{\pi}{\ln 2} \frac{V}{I} \tag{2.6}$$

The four-point probe can measure numerous points of a thin film on a 200 mm wafer to provide a sheet resistance map, usually called the 49 point map. The average sheet resistance obtained gives an approximate value to calculate the resistivity (see equation 2.4). The thickness (t) can be calculated by obtaining a cross section SEM thickness measurement of the thin film. The sheet resistance standard deviation of a 49 point map can provide a measure of film uniformity across the wafer due to the dependence on t and assuming negligible change in film resistivity (see equation 2.4).

## 2.10. Thermal Desorption Spectroscopy (TDS)

TDS is a commonly used method for studying molecular adsorption and surface reactions (35-37). In a basic TDS experiment, the gas molecules are adsorbed on a sample surface at low, room or elevated sample temperatures in a vacuum system. The temperature of the substrate is then increased in a controlled manner while the desorption of products from the surface back into the gas phase is monitored using a quadrapole mass analyzer (QMA). The QMA consists of four parallel shaped electrodes, which serve as mass filters. With application of different electrical fields on the electrodes, selected ions of certain mass-to-charge ratio are allowed to pass to the detector and be quantified. A computer is used to control the whole process of heating and detection of products in TDS. The data obtained from the TDS experiment consists of the intensity of the variation of each recorded mass fragment as a function of temperature.

An adsorbed species present on the surface at low or room temperature may remain almost indefinitely in that state. As the temperature of the sample or substrate is increased in a TDS experiment, there will come a point at which the thermal energy of the adsorbed species is sufficient enough for one of three things to happen. First, the molecular species initially adsorbed may decompose to yield either gas phase or other surface species. Second, the adsorbate can also react with the surface to yield a specific surface compound, or it might diffuse into the bulk of the underlying solid. Thirdly, the reacted or un-reacted species may desorb at a higher temperature from the surface and return into the gas phase. By analyzing the TDS spectrum, overall surface reaction kinetics and mechanisms can be derived. The area under the desorption peak is proportional to the amount of the originally adsorbed species. The kinetics of the desorption process which gives a qualitative picture of the state aggregation of the adsorbed species (i.e. associative or dissociative adsorption) is obtained from the peak profile and the coverage dependence of the desorption characteristics. The position of the peak temperature (where maximum desorption occurs) can be further related to the enthalpy of adsorption of the strength of the binding of the adsorbate to the surface. If there is more than one binding site for an adsorbate, then the TDS will show multiple peaks in the TDS spectrum corresponding to different enthalpies of adsorption for each surface site.

## 2.11. Chemical Vapor Deposition

Beginning in the mid to late 80's, chemical vapor deposition (CVD) became an essential part of ultra large-scale integrated circuit (ULSI) manufacturing. It is widely

used for its superior ability to produce more conformal films (i.e. high step coverage) than the physical vapor deposition method (38). Reproducing precisely the underlying topography of metal, dielectric and semi-conducting films to produce multi-layer metallization architectures promotes CVD as a technique of choice for thin film growth in microelectronic fabrication. In this section, a brief overview of CVD fundamentals and the type of CVD reactor used in chapter 3 (plasma enhanced CVD (PECVD)) will be covered.

CVD is a sequential process that starts from the initial vapor phase, progresses through a series of steady-state sub-processes, and culminates in the formation of a solid film in its final microstructure. The sequence is illustrated in Figure 2.4. Below the following steps describe the process.

1) Diffusion of gas reactants to the surface

2) Adsorption of the reacting species on to surface sites, often after some migration on the surface.

3) Surface chemical reaction between the reactants, usually catalyzed by the surface.

4) Desorption of the reaction by-products.

5) Diffusion of the by-products away from the surface.

6) Incorporation of the condensed solid product into the microstructure of the growing film.

The reaction is usually endothermic and the energy driving the reaction can be supplied by several sources such as thermal, photons and electrons, where thermal energy is the most common.

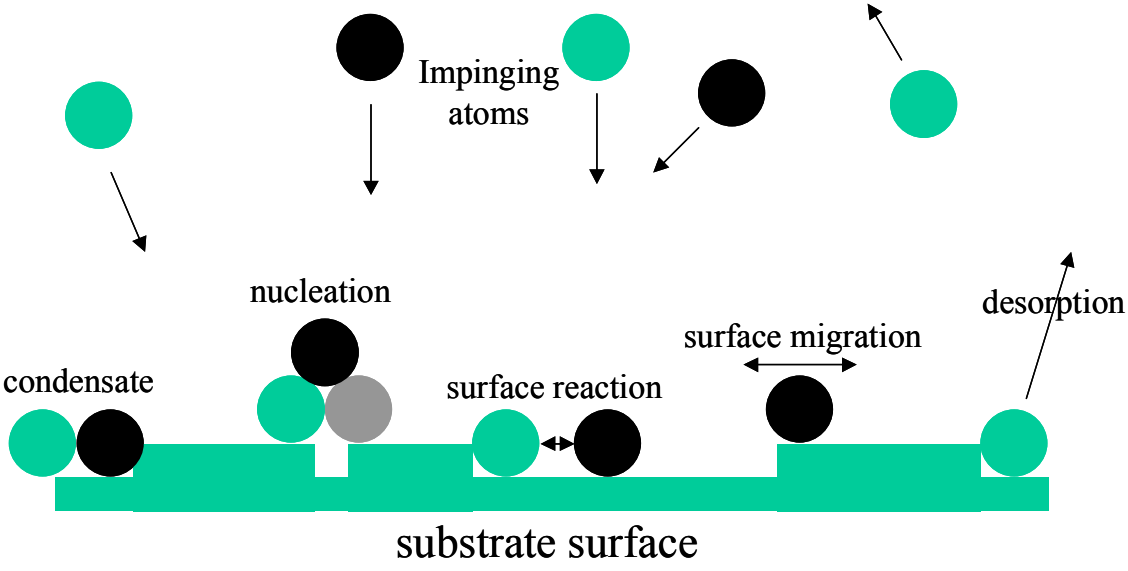


Figure 2.4. The multiple processes occurring in a chemical vapor deposition process that leads to deposition on the wafer.

The rate of deposition is determined by the slowest step in the CVD process. The steps can be grouped into gas-phase processes and surface processes. The gas phase phenomenon critical in the sequential CVD process steps is the rate at which gases impinge on the substrate (step 2). This is modeled by the rate at which gases cross the boundary layer that separates the bulk regions of flowing gas and substrate surface. With minimal impact by gas phase reactions, the transport process occurs by gas-phase diffusion and is proportional to the diffusivity of the gas and concentration gradient across the boundary layer. The surface reaction (step 3) can be represented by a thermally activated phenomenon that proceeds at a rate R:

$$R = R_o e^{(-Ea/kT)} \tag{2.7}$$

where $R_o$ is the collision frequency, $E_a$ is the activation energy in eV, and T is the temperature in $^{o}$K. The terms collision frequency and activation energy arise out of the

concept of an activated complex. Consider the reaction A + B → C where the reaction is hypothesized to occur through a sequence of reactions:

$$A + B \longrightarrow AB^* \longrightarrow C \qquad (2.8)$$

AB* is called the activated complex and is in equilibrium with A and B. An energy diagram of the reaction is shown in figure 2.5, which typically represents a CVD process driven by heating the substrate (thermal CVD). The activated complex is formed by the collision of A and B molecules and has a negligibly short lifetime. It is the potential hill in figure 2.5 that represents the required energy to create the activated complex and is called the activation energy.

From equation 2.7, an increase in temperature results in the increase in surface reaction rate. If a temperature rises high enough for a given surface reaction, the reaction rate exceeds that rate at which reactant species arrive at the surface. The reaction cannot occur any more rapidly than the rate at which reactant gases are supplied to the substrate by mass transport, no matter how high the temperature is increased. Therefore the rate of gas adsorption to the surface (step 2) is termed mass-transport limited and is the rate-limiting step.

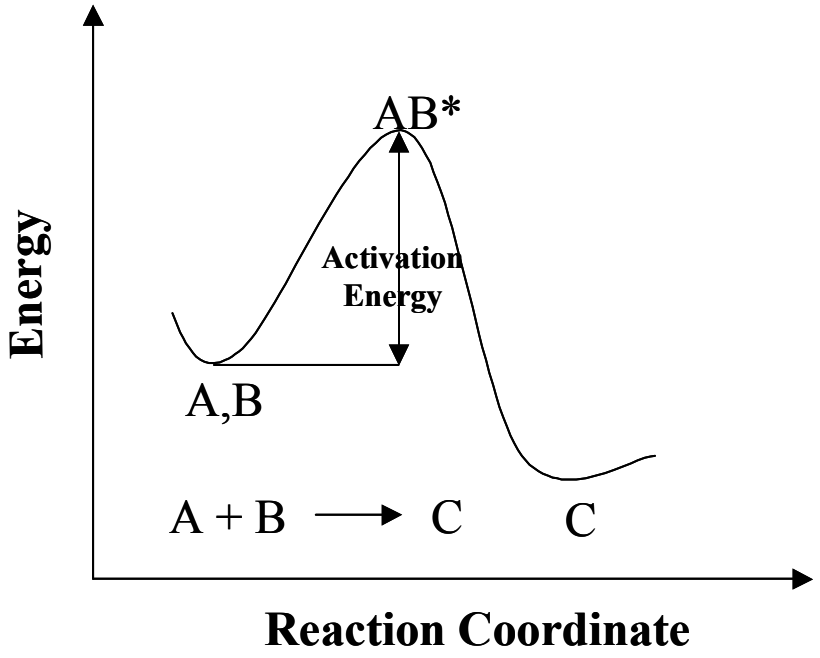


Figure 2.5. An energy diagram of a typical CVD process. The activation of energy of the reaction is the energy needed to overcome the "hill" in order to form products.

With decreasing temperature, the surface reaction decreases and will eventually cause the arrival rate of the reactants to exceed the surface reaction process rate. This is called reaction rate limited and therefore the surface reaction process is the rate-limiting step (step 3). At high temperatures, the deposition is usually mass-transport limited, while at lower temperatures it is surface-reaction rate limited (see figure 2.6). The temperature at which the deposition condition moves from one of these growth regimes to the other is dependent on the activation energy ($E_a$) of the reaction, and the gas flow conditions in the reactor.

In a thermal CVD process, thermal energy is the sole source to initiate and sustain chemical reactions and requires high substrate temperatures (see reaction pathway X, figure 2.5). In the Plasma Enhanced Chemical Deposition (PECVD) process, an RF

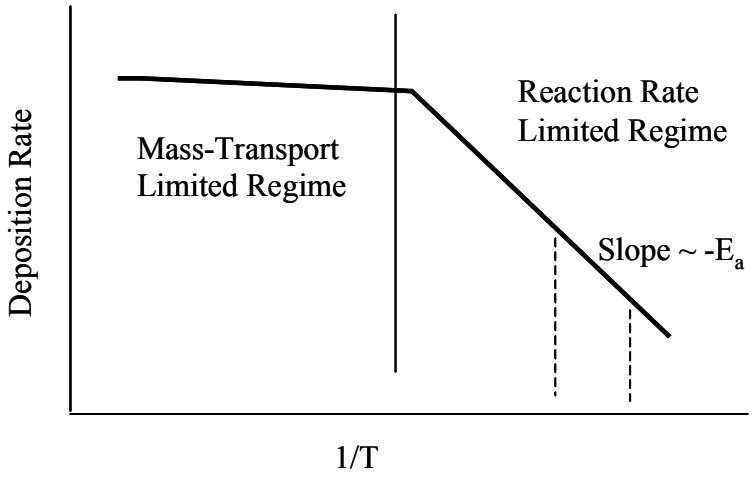


Figure 2.6. Temperature dependence of growth rate for CVD films.

(radio frequency) induced glow discharge is used to transfer energy into the reactant gas. Fig 2.7 illustrates the existence of a new reaction pathway Y, due to the presence of charged precursors generated in a plasma. This lowers the overall activation energy for the reaction. With the lowering of the activation energy through the formation of excited species A* and B* the forward reaction can proceed at lower substrate temperatures. Lower substrate temperature is the major advantage of PECVD because it allows the deposition of material on substrates that would typically destabilize under thermal CVD conditions (e.g. dielectric deposition on an Aluminum substrate above its melting point). Other advantages of PECVD are higher deposition rates (39). Electrons from the plasma collide with reactant gas molecules resulting in gas-phase dissociation and ionization.

This yields more reactive species for substrate reaction and adsorption in contrast to thermal CVD processes where the reactant species are not yielded until migration across the vacuum to the heated substrate. With a high deposition rate, amorphous films are likely produced (40). This is likely where the condensed or nucleated adsorbate is quickly buried under subsequent layers limiting grain growth or periodic atomic ordering (40). High step coverage is also likely with PECVD due to higher surface mobility associated with more energetic plasma generated reactant gas species. (39, 41, see section 1.3.4).

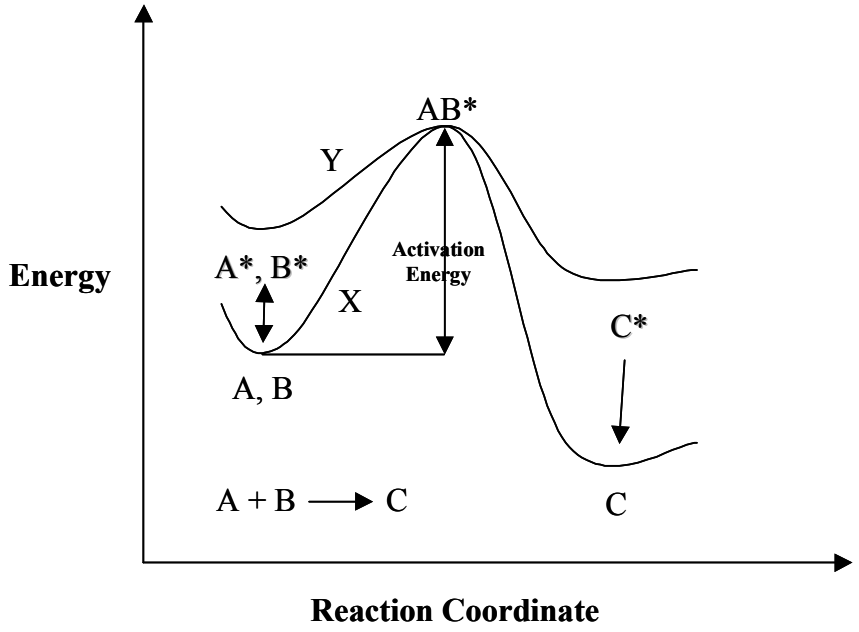


Figure 2.7. Energy change and species formed (X) with a thermal CVD path and (Y) with a plasma CVD path. A* and B* represent excited precursors generated due to a plasma. The plasma reduces the overall activation energy.

## 2.12. Chapter References


(1) Sun, S. C.; Tsai, M. H.; Chiu, H. T.; Chuang, S. H. *Symposium on VLSI Technology Digest of Technical Papers.* **1996**, 46-47.

(2) Park, B. L.; Ko, D-H.; Kim, Y. S.; Lee, M. Y. *Journal of Electronic Materials*. **1997**, *26 (2)*, L1-L5.

(3) Lu, J. P.; Hsu, W. Y.; Luttmer, J. D.; Magel, L. K.; Tsai, H. L. *Journal of the Electrochemical Society*. **1998**, *145 (2)*, L21-L22.

(4) Park, Lee M-B.; Moon, K-J.; Lee, H-D; Kang, H-K; Lee, M-Y. *Conference Proceedings ULSI XII Materials Research Society*. **1998**, 163-167.

(5) Lu, J. P.; Hsu, W. Y.; Luttmer, J. D.; Havemann, R. H. *Conference Proceedings ULSI XII Materials Research Society.* **1998**, 87-93.

(6) Takeyama, M.; Noya, *A*. *Journal of Applied Physics*. **1997**, *36*, 2261-2265.

(7) Cullity, B. D. *Elements of X-ray Diffraction*; Addison-Wesley: Reading, MA, 1956; pp. 1-514.

(8) Azaroff, L. V. *Elements of X-ray Crystallography*; McGraw-Hill: New York, 1968; pp. 1-610.

(9) Goldstein, J. I.; Newbury, D. E.; Echlin, P.; Joy, D. C.; Fiori, C.' Lifshin, E. *Scanning Electron Microscopy and X-ray Microanalysis*; Plenum Press: New York, 1981; pp. 1-673.

(10) Goldstein, J. I.; Yokowitz, H.; Newbury, D. E. *Practical Scanning Electron Microscopy : Electron and Ion Microprobe Analysis*; Plenum Press: New York, 1975; pp. 1-582.

(11) Thornton, P. R. *Scanning Electron Microscopy: Applications to Materials and Device Science*; Chapman and Hall: London, 1968; pp. 1-368.

(12) Murr, L. *Electron and Ion Microscopy and Microanalysis*; Marcel Dekker Inc: New York, 1982; pp. 1-793.

(13) Fryer, J. R. *The Chemical Applications of Transmission Electron Microscopy*; Academic Press: London; New York, 1979; pp. 1-286.

(14) Heidenreich, R. D. *Fundamentals of Transmission Electron Microscopy*; Interscience Publishers: New York, 1964; pp. 1-414.

(15) Marcus, R. B.; Sheng, T. T. *Transmission Electron Microscopy of Si VLSI Devices and Structures*; John Wiley & Sons, Inc.: New York, 1983; pp. 1-217.

(16) Somorjai, G. A. *Introduction to Surface Chemistry and Catalysis*; John Wiley & Sons, Inc.: New York, 1994; p. 390.

(17) Briggs, D.; Seah, M. P. *Practical Surface Analysis*; John Wiley & Sons Ltd: New York, 1983, pp. 1-533.

(18) Carlson, T. A. *Photoelectron and Auger Spectroscopy*; Plenum Press: New York, 1975; pp. 1-417.

(19) Davis, L. E.; MacDonald, N.C.; Palmberg, P. W.; Riach, G. E.; Weber, R. E. *Handbook of Auger Electron Spectroscopy*, *2nd ed.* Physical Electronics: Eden Prairie, MN, 1976; pp. 1-12.

(20) Seah, M. P.; Dench, W. A. *Surface Interface Analysis*, **1979**, *1*, 2.

(21) Muraka, S. P. *Metallization Theory and Practice for VLSI and ULSI*; Butterworth-Heinemann: Boston, MA, 1993; pp. 172, 173.

(22) Larrabee, G.B. *Materials Characterization for VLSI*; Einspruch, N. G.; Ed.; Academic Press: Orlando, FL, 1981; Vol. 2, p. 37.

(23) Walls, J. M. *Methods of Surface Analysis*; Cambridge University Press: New York, 1989; p. 223.

(24) Bennighoven, A. *Secondary Ion Mass Spectrometry : Basic Concepts, Instrumental Aspects, Applications, and Trends*; J. Wiley: New York, 1987; pp. 1-1227.

(25) Williams, P. *Analytical Chemistry*. **1977**, *49*, 1399.

(26) Wolf, S.; Tauber, R. N. *Silicon Processing for the VLSI Era, Volume 1 - Process Technology*; Lattice Press: Sunset Beach, CA, 1986; pp. 608.

(27) Wolf, S.; Tauber, R. N. *Silicon Processing for the VLSI Era, Volume 1 - Process Technology*; Lattice Press: Sunset Beach, CA, 1986; pp. 607.

(28) Somorjai, G. A. *Introduction to Surface Chemistry and Catalysis*; John Wiley & Sons, Inc.: New York, 1994; p. 19, 330, 597, 600-601.

(29) Dror, S. *Scanning Force Microscopy: With Applications to Electric, Magnetic and Atomic Forces*; Oxford University Press: New York, NY, 1991; pp. 1-263.

(30) Cohen, Samuel H. *Atomic Force Microscopy/Scanning Tunneling Microscopy*; Plenum Press: New York, 1994; pp. 1-453.

(31) Tencor FLX-5200h manual # 274488 Rev. B, February, 1995, pp. 9-1 to 9-3.

(32) Wolf, S.; Tauber, R. N. *Silicon Processing for the VLSI Era, Volume 1 - Process Technology*; Lattice Press: Sunset Beach, CA, 1986; pp. 114-118.

(33) Prometrix Auto RS55/tc manuel, # 04-0187 A, 1994, pp. A1 - A9.

(34) Muraka, S. P. *Metallization Theory and Practice for VLSI and ULSI*; Butterworth-Heinemann: Boston, MA, 1993; pp. 3-6.

(35) de Jong, A. M., Niemantverdret, J. W. *Surf. Sci.* **1990**, *233*, 355.

(36) King, D. A. *Surf. Sci.* **1975**, *47*, 384.

(37) Redhead, P. A. *Vacuum*. **1962**, *12*, 203-211.

(38) Muraka, S. P. *Metallization Theory and Practice for VLSI and ULSI*; Butterworth-Heinemann: Boston, MA, 1993; pp. 126-133, 142, 143.

(39) Wolf, S.; Tauber, R. N. *Silicon Processing for the VLSI Era, Volume 1 - Process Technology*; Lattice Press: Sunset Beach, CA, 1986; pp. 168, 171-195.

(40) Wolf, S.; Tauber, R. N. *Silicon Processing for the VLSI Era, Volume 1 - Process Technology*; Lattice Press: Sunset Beach, CA, 1986; pp. 109-113, 168.

(41) Muraka, S. P. *Metallization Theory and Practice for VLSI and ULSI*; Butterworth-Heinemann: Boston, MA, 1993; pp. 228.

# CHAPTER 3

# PROCESS DEVELOPMENT AND CHARACTERIZATION OF PLASMA ENCHANCED CHEMICAL VAPOR DEPOSITION (PECVD) OF $W_2N$ AS A DIFFUSION BARRIER FOR COPPER INTERCONNECTS

## 3.1. Introduction

The integration of copper as an interconnect material for high performance microprocessors offers significant challenges for developing a conformal diffusion barrier technology extendible to below sub micron back-end design rules (1). The adoption of dual inlaid architectures has led to the development of chemical vapor deposition (CVD) barrier processes because of the need for uniform barrier film coverage along the sidewalls of high aspect ratio via/trench structures. In addition, CVD processing can allow deposition of amorphous barrier films which limits grain boundary diffusion mechanisms (see Chapter 2, section 2.11).

Some of the candidates for diffusion barriers of copper are transition metal, metal-nitride, and metal-silicon-nitride materials (ie. Ta, TaN, $W_2N$, TiN, TaSiN, TiSiN, etc.) (2). The ternary phases such as TaSiN (3) and TiSiN (4) have been reported as most robust diffusion barriers. This is primarily because the ternary phases are amorphous and the absence of grain boundaries minimizes potential paths for Cu diffusion. Some of the pure metal and binary barriers reported are Ta based barriers, TiN, and $W_2N$ (2).

A number of processes have been reported for deposition of $W_2N$ films including thermal CVD of tungsten hexafluoride ($WF_6$) and ammonia ($NH_3$) (5-7) and PECVD of $WF_6$ and nitrogen ($N_2$) (8). Thermal CVD results in particulate problems because of gas phase reaction between $WF_6$ and $NH_3$. The particulate problem can be overcome using PECVD of $WF_6$ and $N_2$ (8). Among the advantages of $W_2N$ PECVD is that the $WF_6$ and $N_2$ chemistry allows the use of gas reactants available in high purity at low cost. In addition, PECVD $W_2N$ films have demonstrated excellent diffusion barrier properties for copper (8).

In this chapter, process development and film characterization of a PECVD $W_2N$ barrier will be reported. The $W_2N$ process was characterized at a temperature of 350 $^oC$ over a wide range of process conditions. The process was optimized for stoichiometry (W/N ratio), resistivity and film uniformity, surface roughness and step coverage. The results will show the process capability of PECVD $W_2N$ toward the integration of multi-level dual inlaid Cu structures.

## 3.2. Experimental

### 3.2.1. PECVD $W_2N$ Process Development

The $W_2N$ films were deposited in a commercial PECVD reactor chamber (see figure 3.1). Tungsten hexafluoride ($WF_6$), nitrogen ($N_2$), hydrogen ($H_2$), and argon (Ar) were the reactive gases used to form the $W_2N$ films. Process variables included flow rates (sccm, standard cubic centimeter per minute) for the four gases, deposition temperature, plasma power, deposition pressure, and heater-to-shower head spacing.

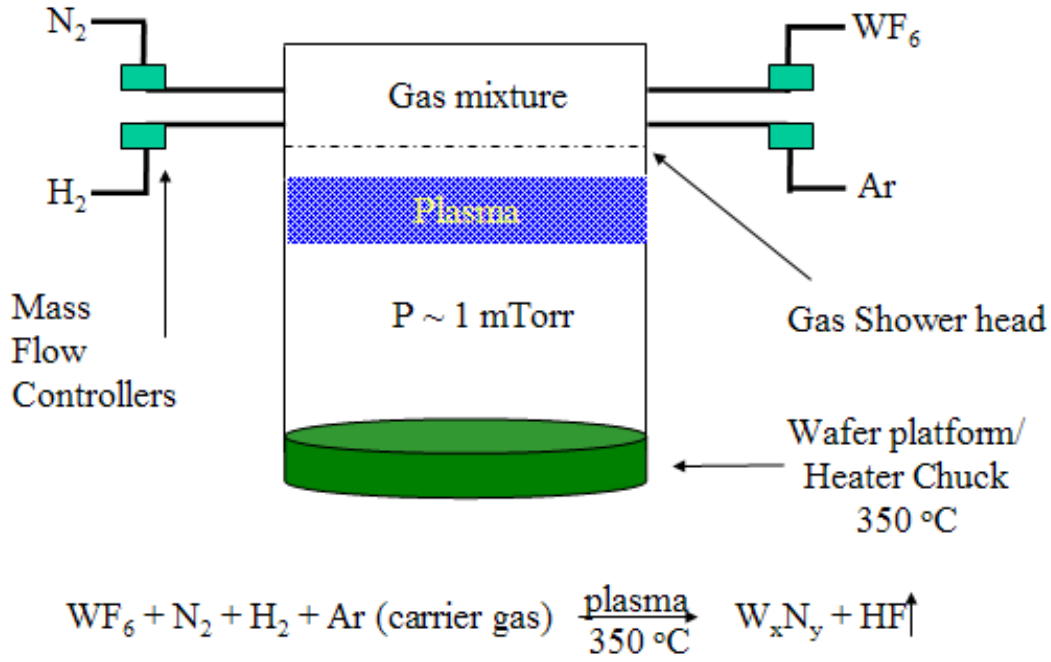


Figure 3.1. A plasma enhanced chemical vapor deposition (PECVD) reactor diagram displaying critical reaction components to the fabrication of $W_xN_y$ films.

For the process development described in this chapter, the wafer temperature was a constant 350 $^oC$ and processing pressure of 1 mTorr. The effect of reactant gases was studied by varying the ratio of their reactant flow rates, such as $WF_6/H_2$, $N_2/H_2$ and $WF_6/N_2$, to simplify understanding of the process variables. The process characterization was done over the remaining parameter space (input factors) by conducting two design of experiments (DOE) (see example in figure 3.2). The optimization was based on the output factors of stoichiometry, film resistivity and uniformity.

### 3.2.2. Film characterization of PECVD $W_2N$ films

Average sheet resistance ($R_s$) and uniformity of $W_2N$ films were calculated based

# Design of Experiment (DOE)

Two-level Full-Factorial Design Pattern  + high value  - low value

| Run | Input Factors | | | | Output |
|---|---|---|---|---|---|
| | $H_2$ | $N_2$ | Ar | Spacing(mm) | $R_s$ and uniformity |
| | Flow rate (standard cubic cm per minute) | | | | |
| 1 | - | - | - | - | ? |
| 2 | + | - | - | - | ? |
| 3 | - | + | - | - | ? |
| 4 | + | + | - | - | ? |
| 5 | - | - | + | - | ? |
| 6 | + | - | + | - | ? |
| 7 | - | + | + | - | ? |
| 8 | + | + | + | - | ? |
| 9 | - | - | - | + | ? |
| 10 | + | - | - | + | ? |
| 11 | - | + | - | + | ? |
| 12 | + | + | - | + | ? |
| 13 | - | - | + | + | ? |
| 14 | + | - | + | + | ? |
| 15 | - | + | + | + | ? |
| 16 | + | + | + | + | ? |
| 17 | c | c | c | c | ? |

Figure 3.2. A typical design of experiment scheme used for $W_2N$ development. Input factors consisted of $H_2$, $N_2$, and Ar flow rate (sccm) and wafer to gas shower-head spacing. In this figure, output factors were sheet resistance and uniformity. Film stoichiometry was also an output factor for other input schemes. Positive symbols for input factor pertains to a chosen unit maximum and negative symbol a unit minimum. A center point represented by c is the unit midpoint value. The output factors are dependent on the combination of input factors. The intent of the DOE is to explore the experimental space (input factor combinations) to achieve the ideal or optimized output factors.

on a 49 point measurement (four-point probe, see section 2.9) on each wafer and was used to calculate the resistivity ($\rho$) of the $W_2N$ films. As shown in figure 3.3, the resistivity of the $W_2N$ films was calculated by multiplying the average sheet resistance ($R_s$) by the average $W_2N$ SEM thickness (3 measurements across wafer, edge, midpoint,

and center). The stress measurements were done at a $0^o$ and $90^o$ relative to the wafer notch to determine directional dependence of stress in the film. The step coverage

$$\rho = R_s \text{ x film thickness (x)} \quad (3.1)$$

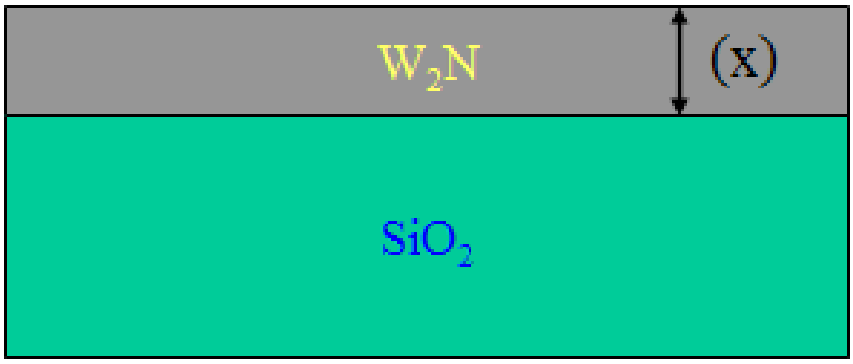


Figure 3.3. Obtaining resistivity (ρ) of the $W_2N$ diffusion barrier. SEM cross sectional analysis of a $W_2N$ / $SiO_2$ stack (200 mm wafer) is performed to achieve the average $W_2N$ thickness. The average thickness (edge, midpoint, and center) is then multiplied by the average sheet resistance (49 point, four point probe Rs measurement) of the $W_2N$ film.

of the $W_2N$ films was studied using cross section scanning electron microscopy (SEM) by measuring film thickness at the top surface as well as along the sidewalls and bottom of the feature.

Film stoichiometry was studied by Auger electron spectroscopy (AES) depth profile. The elements analyzed were W, N, F, O and Si. Among them, W, N, and F are incorporated in the film due to process gases while Si is analyzed to determine $W_2N$ /TEOS interface. The acronym TEOS stands for tetraethoxysilane and is a precursor used in CVD to deposit the dielectric film silicon oxide ($SiO_2$). When the TEOS acronym is used, it represents the silicon oxide ($SiO_2$) film that was formed using the TEOS

precursor. The O can be incorporated upon air exposure if the PECVD $W_xN$ film has a porous microstructure.

Film morphology was studied by cross-section transmission electron spectroscopy (TEM) which allows high resolution imaging of the material. The samples submitted for TEM included $W_2N$ (~200 Å) on TEOS followed by PVD Cu deposition on $W_2N$. The stack was then annealed at 390 $^oC$ for 3 hours in forming gas ($N_2/H_2$ gas mixture). The samples were imaged for barrier morphology, interface interactions and presence of Cu in the TEOS layer to determine Cu diffusion. Selective area electron diffraction (SAED) was also performed for barrier crystallinity. The SIMS technique was used to study the $W_2N$ barrier property for Cu diffusion. The SIMS analysis can allow Cu detection to parts per million (ppm) levels in the TEOS layer.

The phase of the $W_2N$ films was confirmed by normal coupled XRD scan. Film thickness of the $W_2N$ for XRD analysis ranged from 200-500 Å deposited on a TEOS under layer. The diffraction peak maximum represents the film phase and the full width half maximum (FWHM) suggests an order of crystallinity (9). Broader peaks (larger FWHM) are usually indicative of films with less crystallinity, while sharp or narrower peaks represent more crystalline or textured films. It must be understood that XRD alone should not be used to represent the crystalline order of a film, but rather as complementary to an electron diffraction technique (9).

The surface roughness was quantified by atomic force microscopy (AFM). The sample thickness of $W_2N$ ranged from 200-500 Å on a TEOS under layer. The AFM was done over an area of 1 x 1 μm square. The roughness of the $W_2N$ films on the side wall

of the via and trench structures was qualitatively determined by high resolution SEM cross-sections.

The adhesion of Cu on $W_2N$ films and $W_2N$ films to TEOS was studied by scratch tape peel test. The samples included physically vapor deposited Cu (500 Å) on $W_2N$ (200-500 Å) on a TEOS under layer. The samples were then annealed at 390 $^oC$ for 30 minutes.

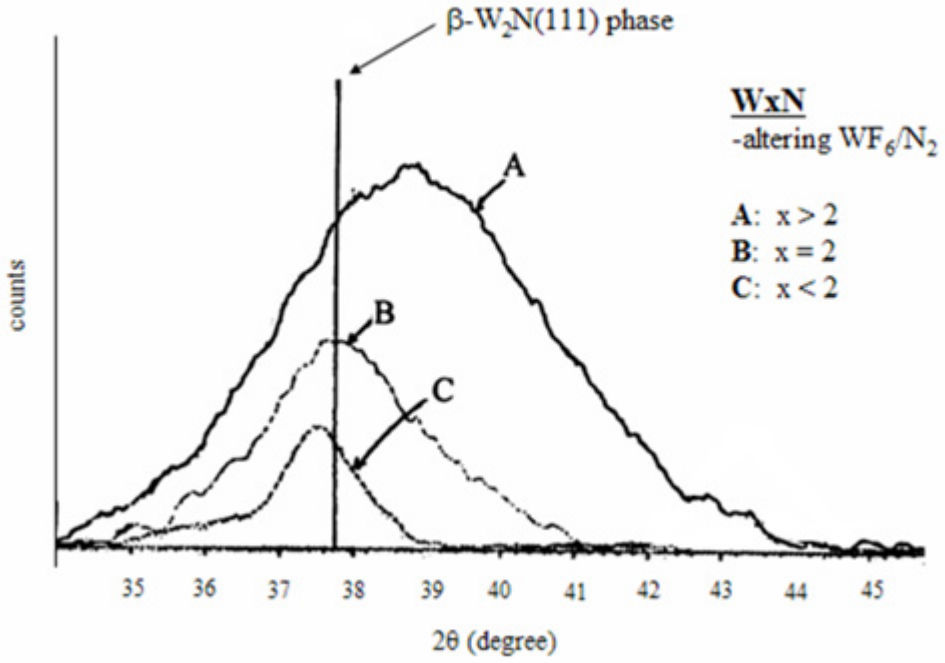


Figure 3.4. X-Ray diffraction (XRD) Plot (normal coupled scan) of $W_xN$ films deposited with varying $WF_6/N_2$ flow rate ratios. Each plot represents the film phase characteristics.

## 3.3. Results

The PECVD $W_2N$ process was optimized by conducting two DOE's. The first DOE was performed to achieve a stoichiometric $W_2N$ film. The W/N ratio in the deposited film was dependent on the ratio of the $WF_6/N_2$ flow rates. The W/N ratio range

was explored by altering the flow rates and a number of $W_xN$ films were deposited and analyzed with XRD. Figure 3.4 shows an XRD plot as a function of the ratio of $WF_6/N_2$ flow rates. In this plot, a vertical line indicates the location of the β-$W_2N$ (111) diffraction peak. Any peak to the right of this line (A) represents a $W_xN$ film with $x > 2$

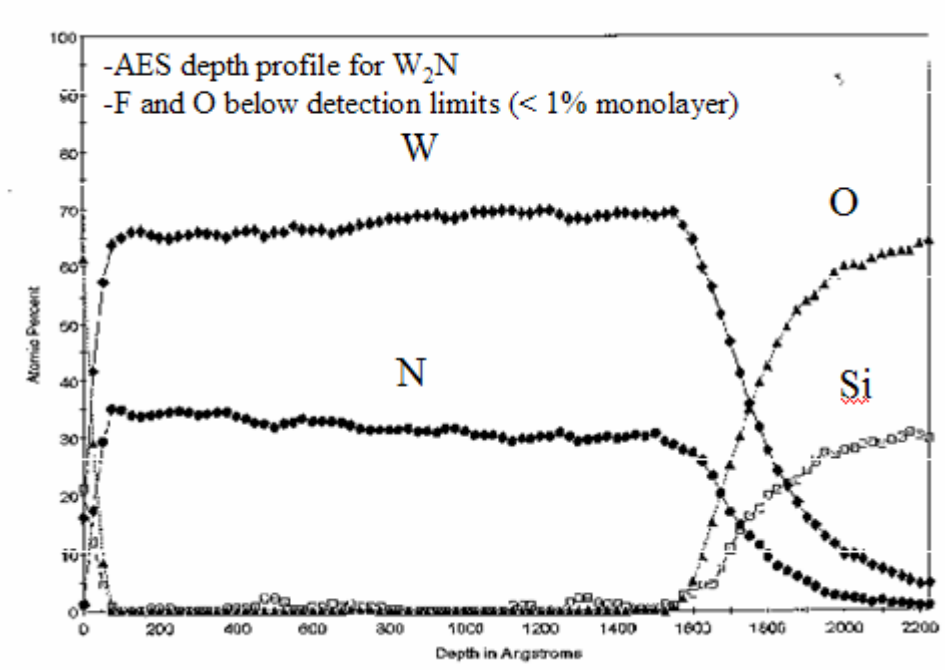


Figure 3.5. Auger electron spectroscopy depth profile for a $W_2N$ (1500 Å)/$SiO_2$(10000 Å)/Si film stack. Oxygen and fluorine levels are below the detection limits).

and peaks to the left (C) of the vertical line represent $x < 2$. For the flow conditions B, a β-$W_2N$ phase film is achieved. This was also confirmed by AES depth profile analysis. Figure 3.5 shows that the W/N ratio is nearly 2:1 with O and F below detection limit (< 1% monolayer). The XRD plot also shows that all peaks are broad and range over several degrees of diffraction angle suggesting amorphous film property with a degree of (111) orientation.

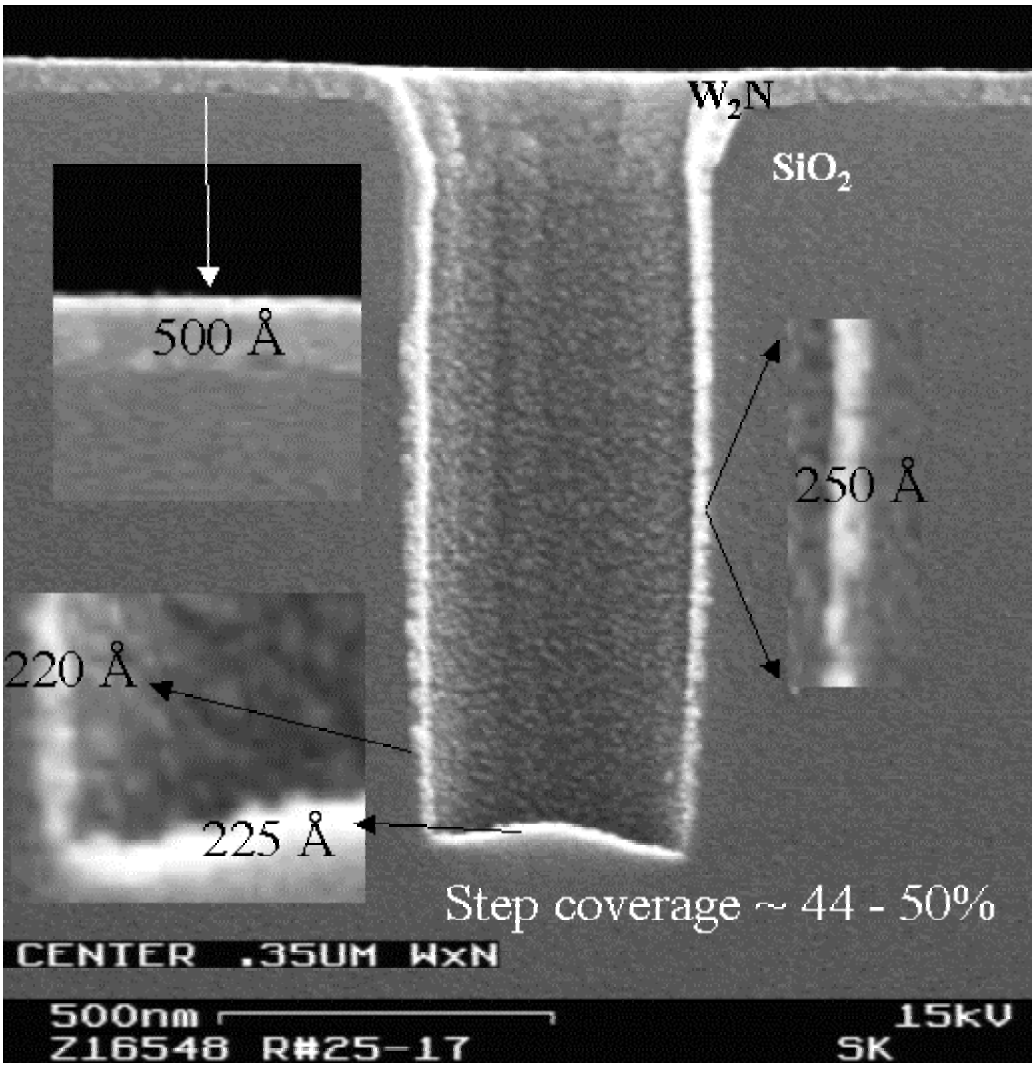


Figure 3.6. A $W_2N$ deposited film (lighter regions) over an inlaid patterned $SiO_2$ film with a 3:1 aspect ratio at 0.35 um. A step coverage of 44 to 50% was achieved.

The second DOE optimized the $W_2N$ film for uniformity (see figure 3.2) and low sheet resistance to achieve low resistivity (see figure 3.3). The film resistivity for the $W_2N$ films ranged from ~270-300 μohm-cm with film uniformity below 3% (standard

deviation of sheet resistance using four point probe measurement profile across an 8 inch diameter wafer, see Chapter 2 section 2.9 for details).

The stress in the optimized $W_2N$ films ranged from 400-700 MPa (tensile) and was found to be independent of the direction ($0^o$ vs. $90^o$) of stress measurement along the wafer. No peeling was observed during scratch tape peel testing for $W_2N$ /TEOS and Cu/ $W_2N$ interfaces before and after anneal (390 $^oC$, 30 minutes) demonstrating good

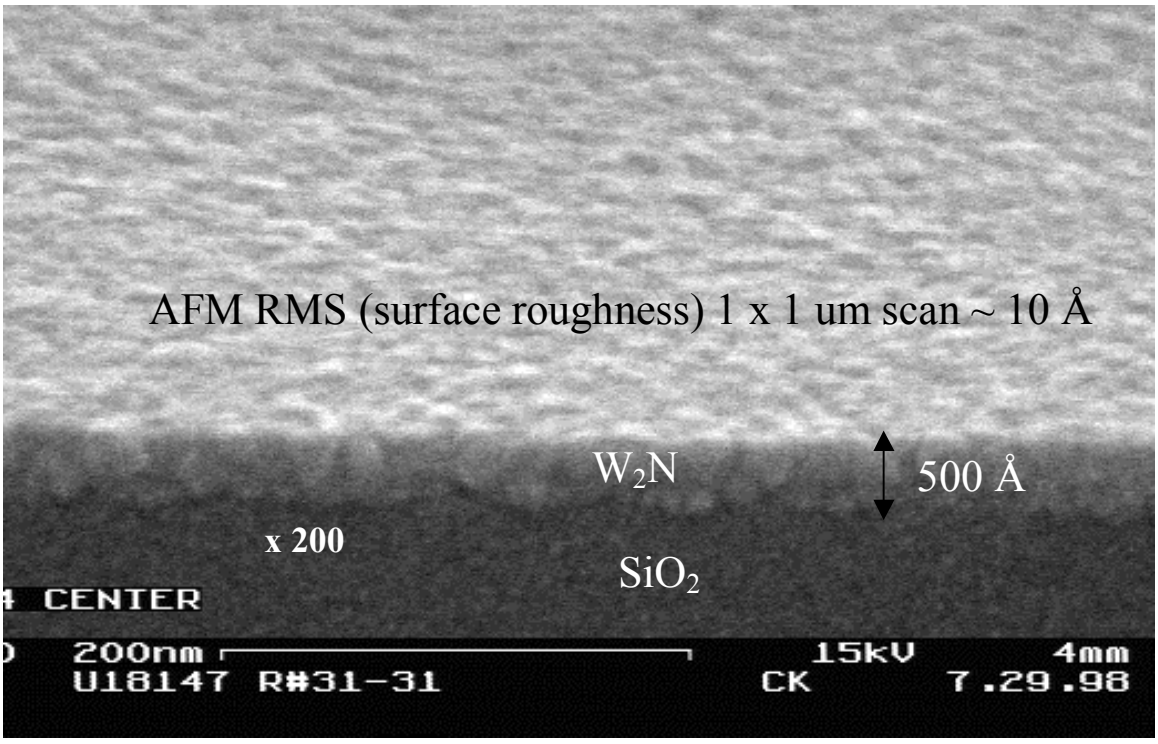


Figure 3.7. SEM tilt image of a $W_2N/SiO_2/Si$ film stack. Visually, the $W_2N$ film is smooth and dense. Surface Atomic Force Microscopy (AFM) root mean square (RMS) measurements were ~ 10 Å on 1 x 1 um scan.

adhesion properties. A high step coverage of ~44-50% was obtained for $W_2N$ films over a 0.35 um via with an aspect ratio of 3:1 (see figure 3.6). Surface roughness measurements (root mean square values) on a 1 x 1 um AFM scan of a $W_2N$ (500 Å

thick)/$SiO_2$/Si film stack (flat, blanket test wafer) was ~10 Å. Figure 3.7 shows SEM measurements demonstrating the smooth surface and dense like appearance of the film.

Copper diffusion barrier properties of $W_2N$ were studied by secondary ion mass spectroscopy (SIMS) analysis. Figure 3.8 represents SIMS depth profile of Cu diffusion through a $W_2N$ (200 Å) film showing that Cu concentration dropped sharply at the $W_2N$/TEOS interface. This supports that the Cu did not diffuse through the barrier after annealing at 390 $^oC$ for 3 hours.

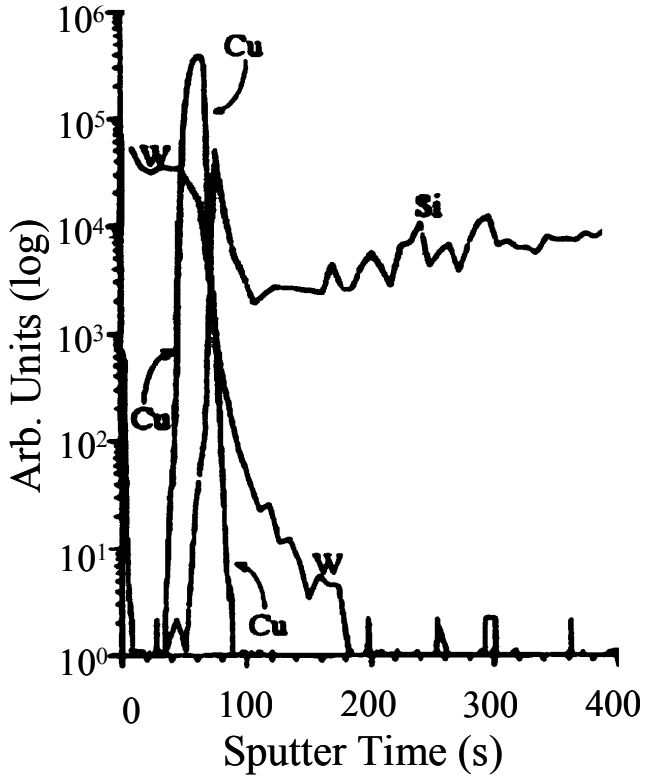


Figure 3.8. Secondary ion mass spectroscopy of a Cu (2000 Å / $W_2N$ (200 Å)/ $SiO_2$ film stack annealed to 390 $^oC$ for three hours. Prior to SIMS profiling, the top layer of Cu was removed with nitric acid. Thus, the SIMS profile was performed on $W_2N$/ $SiO_2$ where Cu, W, and Si concentrations were measured.

The morphology of $W_2N$ film was studied by TEM images. The high resolution TEM images showed presence of some nano-crystallites ranging from 20-40 A and showed random orientation. Selective area electron diffraction (SAED) of the barrier showed a diffused ring pattern, again supporting an amorphous morphology (see figure 3.9 a). The TEM images also showed the absence of Cu in the TEOS film consistent with the SIMS results that $W_2N$ film suppressed Cu diffusion during anneal (see figure 3.9 b).

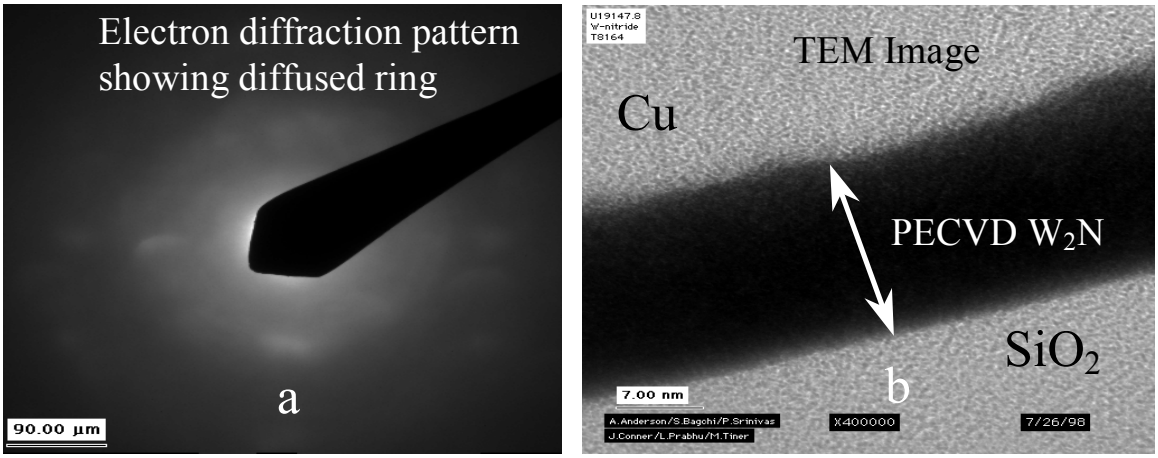


Figure 3.9. a) Selective area electron diffraction (SAED) of the $W_2N$ (200 Å) barrier showing a diffuse ring pattern. b) Transmission electron microscopy (TEM) of a Cu (2000 Å)/ $W_2N$ (200 Å)/TEOS film stack after a 3 hour anneal.

## 3.4. Summary and Conclusions

Integration of dual inlaid Cu interconnects requires development of a conformal diffusion barrier technology. In this chapter, process development and film characterization have been presented for PECVD $W_2N$ films for barrier applications. The process was characterized at a wafer temperature of 350 $^oC$ over a wide range of process conditions ($N_2$, $H_2$, Ar, $WF_6$ flow rates, deposition pressure, plasma power and heater to

showerhead spacing). The $W_2N$ phase was successfully deposited. The optimized films had a resistivity of ~270-300 μohm-cm with a film uniformity of ~3% and a < 10 Å surface roughness. For Cu metallization architectures that use 0.35 μm vias at a 3:1 aspect ratio, typical diffusion barrier resistivity requirements should fall below 800 μohm-cm (10). For 200 mm technology, lithographic imagers require film uniformities to be < 5% (11). The $W_2N$ films produced were amorphous as measured by XRD and TEM. Achieving amorphous films limits grain boundary diffusion pathways (see section 1.3.2). Stress measurements of $W_2N$ films were 400-700 MPa and are 3 times less than stress imposed by TiN and Ta films (2). A 200 Å thick film exhibited excellent barrier properties for Cu diffusion after a 390 $^oC$/3 hr anneal. This demonstrates that the $W_2N$ layer is inert to Cu and inhibits the $Cu/SiO_2$ interaction (11,12). Step coverage of PECVD $W_2N$ films in the range of 44-50 % were achieved for a 0.35 um via with an aspect ratio of 3:1.

The ideal Cu diffusion barrier and adhesion promoter requirements described in sections 1.3.1 (good adhesion, no peeling), 1.3.2 (amorphous character, Cu inter-diffusion resistance), 1.3.3 (resistivity < 800 μohm-cm and low thickness, < 1000 Å)., 1.3.4 (good conformality ~ 50% step coverage through CVD) , 1.3.5 (good uniformity < 5%) and 1.3.6 (low stress < 2100 MPa) have been met for $W_2N$ films characterized in this chapter. From section 1.3.1, the question of Cu adhesion with $W_2N$ is still questionable due to the qualitative nature of the scratch tape peel test. An investigation into the Cu growth modes on the $W_2N$ layer would characterize metal-substrate interaction strength. Also, the critical temperatures at which Cu dewets or "balls up", diffuses or desorbs from

the $W_2N$ surface has not been characterized and is critical toward determining the limits of $Cu/W_2N$ compatibility. In the next chapter, Auger electron spectroscopy and thermal desorption spectroscopy will be used to characterize these items and complete the investigation of $W_2N$ as an adhesion promoter/diffusion barrier for Cu.

## 3.5. Chapter References


(1) International Technology Roadmap of Semiconductors. 1999.

(2) Wang, S-W. MRS Bulletin. August, 1994, p. 30.

(3) Kolawa, E.; Pokela, P. J.; Reid, J. S.; Chen, J. S.; Ruiz, R. P.; Nicolet, M-A. *IEEE Electron Device Letters*. **1991**, *12 (6)*, 321.

(4) Reid, J. S.; Sun, X.; Kolawa, E.; Nicolet, M. A. *IEEE Electron Device Letters.* **1994**, *15 (8)*, 298.

(5) Rossnagel, S. M. *Materials Research Society.* **1995**, *354*, 503.

(6) Nakajima, T.; Watanabe, K.; Watanabe, N. *Journal of the Electrochemical Society*. **1996**, *134*, 3175.

(7) Marcus, S. D.; Foster, R.F. *Thin Solid Films*. **1993**, *236*, 333.

(8) Lu, J. P.; Hsu, W. Y.; Hong, Q. Z.; Dixit, G. A. *Advanced Metallization and Interconnect Systems for ULSI Applications in 1997*. Materials Research Society: Warrendale, PA, 1998; p. 87.

(9) Private Conversations with XRD experts Ajay Jain, Ph D (Intel Corporation, Santa Clara, CA) and Juan Dominguez (Intel Corporation, Hillsboro OR)

(10) Takeyama, M.; Noya, A. *Jpn. J. Appl. Phys*. **1997**, *36*, 2261-2266.

(11) Muraka, S. P. *Metallization Theory and Practice for VLSI and ULSI*; Butterworth-Heinemann: Boston, MA, 1993; pp. 70-74.

(12) McBrayer, J. D.; Swanson, R. M.; Sigmon, T. W. *Journal of the Electrochemical Society*, **1986,** *133*, 1243.

# CHAPTER 4

# CU WETTING AND INTERFACIAL STABILITY ON CLEAN AND NITRIDED TUNGSTEN SURFACES

## 4.1. Introduction

Tungsten nitride is of significant interest as a barrier for Cu diffusion in ultra large-scale integration (ULSI) (1-14). Understanding the nature or properties of a Cu-barrier interface is important toward screening compatible materials for ULSI. Such properties include metal-substrate interaction strength and the critical temperature at which these interfaces destabilize. A method for investigating such interfaces is the application of surface science techniques in ultra high vacuum (UHV). Vacuum pressures on the order of $1.0 \times 10^{-10}$ Torr allow controlled experiments, resolving contamination issues that can affect the fundamental chemical and physical properties at interfaces. Specific surface science techniques such as Auger electron spectroscopy (AES) can be used to examine the growth/nucleation behavior and thermal stability of metals on surfaces (15-18). Understanding the growth/nucleation behavior is important towards characterizing metal-substrate interaction strength. Investigating interfacial thermal stability is important to determine the critical temperature at which metals dewet or "ball up", diffuse or desorb from the surface.

In this investigation, Auger electron spectroscopy (AES) and thermal desorption spectroscopy (TDS) were used to: 1) characterize the interfacial strength of copper (Cu) to clean (W) and nitrided ($W_xN$/W) polycrystalline tungsten foil and 2) determine the critical temperatures at which these interfaces destabilize.

## 4.2. Experimental

Experiments were performed using a turbo molecularly pumped stainless steel ultra-high vacuum (UHV) system equipped for Auger electron spectroscopy (AES) and thermal desorption spectroscopy (TDS) (19). After bakeout, the base pressure was 1.0 x $10^{-10}$ Torr. The chamber pressure was monitored using a nude ion gauge calibrated for dinitrogen and mounted out of line of sight of the sample in order to minimize electron-induced chemistry at the sample surface. The sample used was a 10 x 6 mm, 0.5 mm thick polycrystalline tungsten foil (99.98 % purity) spot welded to two tantalum leads. The sample temperature was monitored by a chrome-alumel thermocouple spot-welded to the back of the sample. The sample temperature was varied between 300 K and 1430 K by resistive heating. The tungsten foil was cleaned by repeated cycles of $Ar^+$ sputtering and annealing at 1430 K. Sample cleanliness was determined by AES. The sample was considered clean with oxygen, nitrogen and carbon atomic concentrations $\leq$ 3 %, $\leq$ 1% and $\leq$ 1% respectively (20).

Auger spectra were acquired in the derivative [dN(E)/d(E)] mode using a commercial cylindrical mirror analyzer, lock-in amplifier (4 eV peak-to-peak modulation) and acquisition software. TDS spectra were recorded with a linear heating rate of 12 K $s^{-1}$ using a quadruple mass spectrometer collimated for line-of-sight to the

sample. The spectrometer was interfaced to a personal computer capable of recording up to ten different atomic mass unit (amu) settings during a single run.

The nitrided tungsten surface was prepared by direct-dosing a hot tungsten foil (~750 K) with anhydrous ammonia (99.99 purity%) for 30 minutes at 1.0 x $10^{-7}$ Torr. Accurate exposures could not be measured for ammonia due to its long residence time on the chamber walls. To avoid residual ammonia contamination after dosing, the foil was further annealed (~90 minutes) until the background pressure was achieved. Films prepared in this way have been characterized by Peng and Dawson with the use of TDS (21). Thermal Desorption Spectra of these films demonstrated top down surface stoichiometries of $W_2N_3H(\eta)$, $WN(\delta)$, and $W_2N(\beta)$ identified by $N_2$ desorption maxima at 975 K, 1100 K, and 1350 K, respectively. Figure 4.1 displays similar $N_2$ desorption maxima for the temperature range (800 – 1350 K) where the predominant phase order follows $WN(\delta)$ ($T_{max}$ ~ 1012 K) > $W_2N(\beta)$ ($T_{max}$ ~1330 K). The data rule out the presence of $W_2N_3H(\eta)$ because of the absence of $H_2$ desorption for all temperatures (300 – 1400 K). Reports (22) of a decomposition temperature for $W_xN$ films (~ 1073 K) also support the predominance of the $WN(\delta)$ phase. For the purpose of this chapter, the $W_xN$ designation will reflect the nitride overlayer consisting of $WN(\delta)$ and $W_2N(\beta)$. The nitride overlayer thickness was estimated by measuring the attenuation of the contaminant O signal on the W metal surface with increasing nitride growth. The thickness of the nitride layer (d) leads to the attenuation of the oxygen signal according to (23):

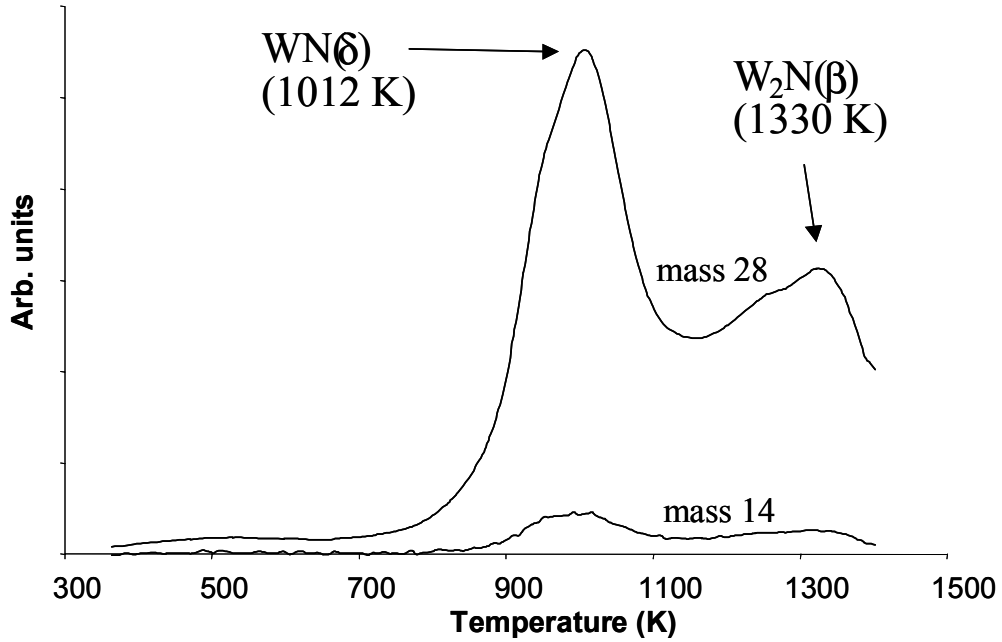


Figure 4.1. Temperature Desorption Spectroscopy of the nitrided tungsten overlayer ($W_xN$/W(poly). Peak assignments derived from ref. 21.

$$I = I_o e^{-d/\lambda} \tag{4.1}$$

where $\lambda$ is the O (KVV) mean free path ($\lambda$ = 15.5 Å) (24) and $I_o$ (I) is the intensity before (after) nitride overlayer formation. A nitride overlayer thickness of 7.5 Å was estimated by this method.

Copper was deposited using a commercial e-beam evaporator equipped with a flux monitor and shutter for obtaining precise coverages. To avoid contamination issues, the evaporator was outgassed at least 10 minutes before use. Monolayer coverages refer to the deposition time required for one complete Cu layer on the clean W surface described in more detail in section 3.1. All error bars refer to the standard deviation from the average of three repeated experiments.

Copper growth modes on tungsten and nitrided tungsten surfaces were studied by plotting Auger Cu/W, WxN intensity ratio as a function of Cu deposition time (Auger signal vs. deposition time plot, AS-t). As outlined by Rhead (15), this analysis method uses break points (or lack thereof) in an AS-t plot to represent two or three dimensional growth modes. The break point in an AS-t plot represents the completion of a deposited layer across a substrate. The adsorbate-substrate interaction is strong and the sharp change is due to the attenuation of the underlying substrate signal. This is termed two

## 4.3. Results and Interpretation

### 4.3.1. Cu on Clean vs. Nitrided W Surfaces

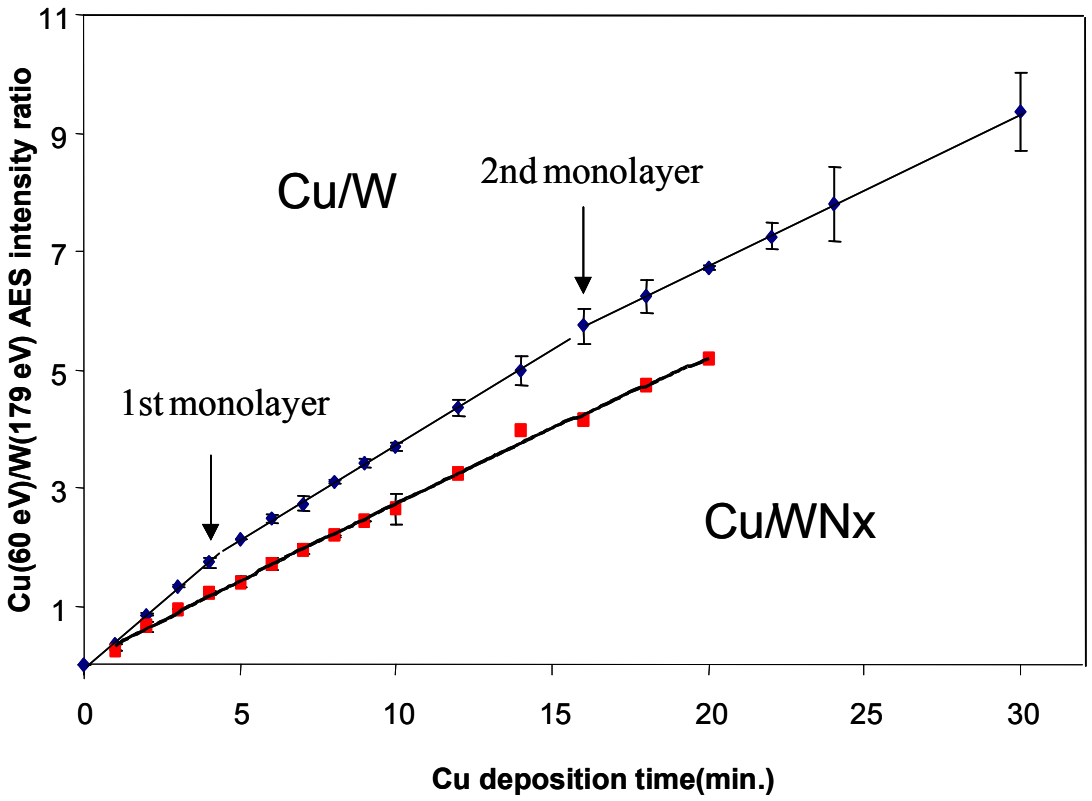


Figure 4.2. Cu (60 eV)/W (179 eV) Auger intensity ratio vs. time plot for W and $W_xN$ surfaces.

dimensional growth. AS-t plots without break points represent three dimensional growth. Adsorbates tend to coalesce rather than interact with the substrate. With less coverage over the substrate, the attenuation effect is much lower.

Auger adsorbate ($i_A$) to Auger substrate ($i_S$) signal ratio vs. time plots (($i_A$/ $i_S$) - t plots) (25) for the room temperature deposition of copper on clean and nitrided tungsten are presented in figure 4.2. Each data point represents the average of three separate Auger peak-to-peak intensity ratio measurements for Cu (60 eV) to W (179 eV), plotted as a function of deposition time (minutes).

For the clean tungsten surface, the Cu (60 eV) /W (179 eV) Auger intensity ratio increases linearly as a function of copper deposition time up to 4 minutes. At 4 minutes, the slope breaks and remains linear until another break is observed at 16 minutes. From 16 onward the plot is also linear. The changes or breaks in the slope at 4 and 16 minutes represent the completion of the 1$^{st}$ and 2$^{nd}$ copper overlayers, respectively (15). For copper depositions of 4 minutes, TDS measurements (figure 4.3) demonstrate a discrete copper desorption peak (1220 K) corresponding to the desorption of Cu from the W surface. For t > 4 minutes, multilayer desorption is observed (26). Both the Auger and TDS data support a strong Cu-W interaction or wetting of the copper on the clean tungsten substrate. The Cu/W atomic ratio can be derived from relative Auger intensities according to established methods (27). The Cu/W atomic ratio at the first break (figure 4.2) is 1.1, consistent with the formation of a monolayer.

For copper deposited on the nitrided tungsten surface, no changes or breaks in the slope are observed (figure 4.2). The copper Auger signal on the nitrided tungsten is

considerably lower than that observed for the Cu grown at equivalent deposition times on the clean W surface (figure 4.2). If the growth behaviors for copper on clean and nitrided tungsten were the same, the Cu/nitride data points (i.e., Cu/W intensity ratios vs. deposition time) should lie above the corresponding points for the non-nitrided surface since nitrogen adds to the attenuation of the bulk tungsten signal. The data in figure 4.2 are indicative of Cu island formation on the nitrided surface, indicating poor Cu-nitride interaction or non-wetting of the copper on the $W_xN$ surface.

### 4.3.2. Cu Thermal Stability on Clean vs. Nitrided W Surfaces

Thermal stability measurements for 1 monolayer of copper deposited at room

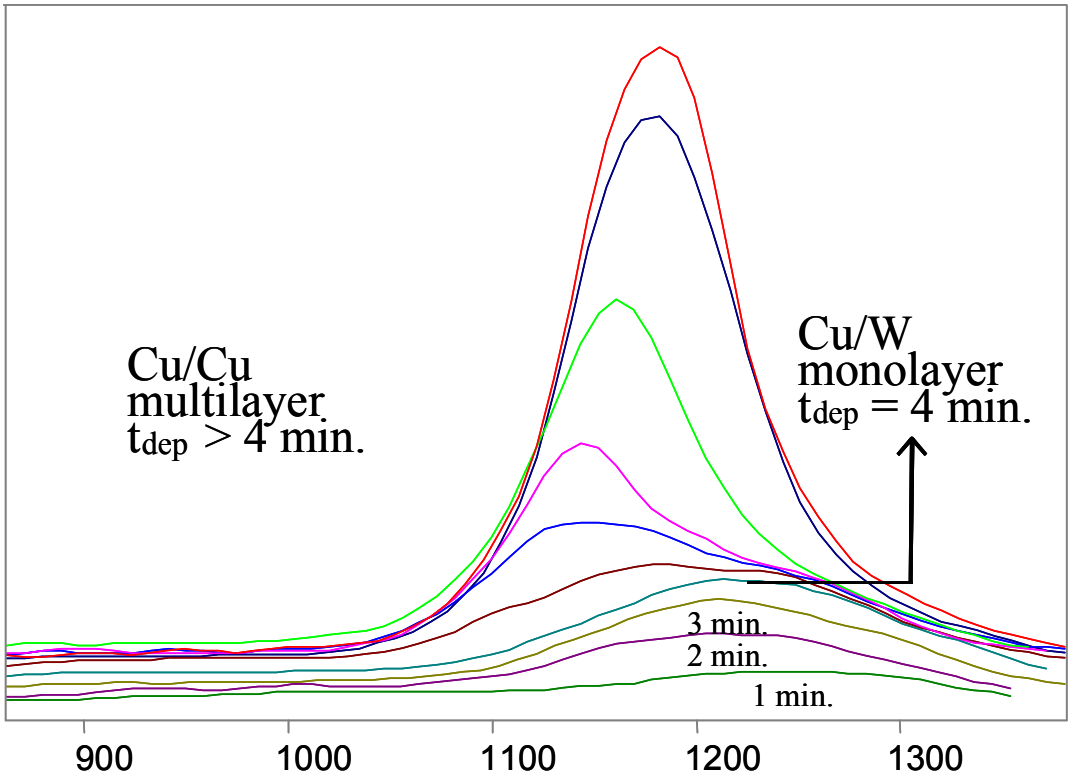


Figure 4.3. TDS data for various coverages of Cu on clean W.

temperature on clean and nitrided tungsten are presented in figure 4.4 a and 4.4 b, respectively. The Cu (920 eV) / W(179 eV) Auger intensity ratios (left y-axis) are plotted as a function of temperature. The Cu(920 eV)/Cu (60 eV) Auger intensities vs. temperature are also plotted (right y-axis). Each data point was obtained after a 15 minute anneal to allow for equilibration. Experiments involving AES intensity vs. annealing time (data not shown) demonstrated an equilibration time from 1 to 5 minutes for all temperatures.

The variation in Auger intensity or Auger intensity ratios reflects changes in surface concentration. A decrease in the Cu/W intensity ratio could result from either Cu diffusion or dewetting (islanding) from the W surface (Cu desorption will not occur below 1000 K) (26). A useful method for examining copper diffusion into the bulk substrate consists of plotting the Cu (920 eV)/Cu (60 eV) Auger intensity ratio as a function of temperature. Because the mean free path of the Cu (60 eV) transition ($\lambda$ = 6.4 Å) is shorter than that of the Cu (920 eV) transition ($\lambda$ = 26.6 Å), the Cu (60 eV) Auger signal is preferentially attenuated (24). The degree of attenuation (At) of an Auger signal of Cu that is covered by an overlayer of thickness d can be calculated using equation

$$At = 1 - I/I_o \qquad (4.2)$$

where $I/I_o$ is defined in equation (4.1). If Cu is covered by a 7 Å overlayer after it has diffused, the Cu (920 eV) and Cu (60 eV) signals are attenuated by ~23 % and ~66 %, respectively. Since the intensity of the Cu (60 eV) decreases markedly upon Cu diffusion into the bulk, the Cu (920eV)/Cu (60 eV) intensity ratio increases. This effect has been previously demonstrated for Cu diffusion into $AlO_x$ films (16). Conversely, dewetting

should result in no significant preferential attenuation for island sizes $\leq \lambda_{60\ eV}$ or 6.4 Å. Therefore, Cu diffusion into the bulk would be indicated by a decrease in the Cu/W data

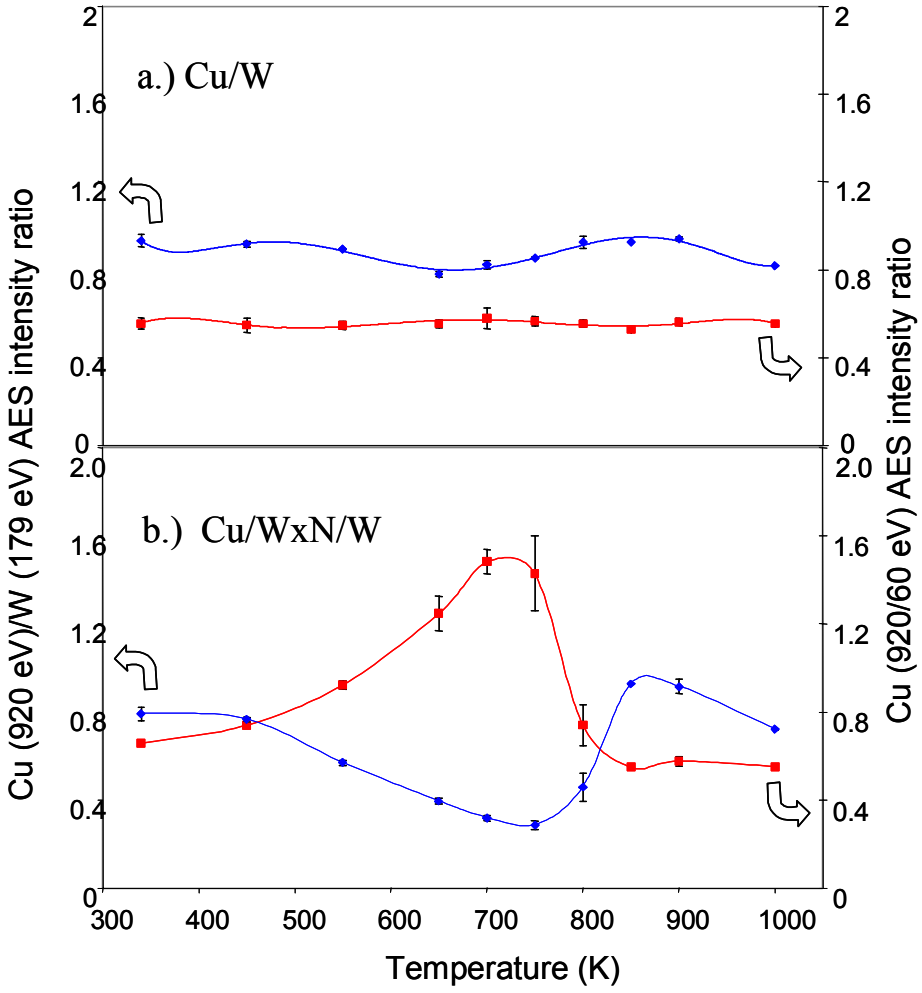


Figure 4.4. Cu (920 eV) /W (179 eV) (left axis) and Cu 920 eV /60 eV (right axis) Auger intensity ratio vs. temperature for: a) Cu(1 ML)/W b) Cu (1 ML)/$W_xN$/W.

and an increase in the Cu (920 eV)/Cu (60 eV) ratio. Conversely, a decrease in the Cu/W ratio with little or no change in the Cu (920 eV)/Cu (60 eV) ratio would indicate dewetting.

For the copper (1 ML) clean tungsten interface, a stable Cu/W interface is observed for the temperature range of 300 to 1000 K. No significant deviations or changes in the Cu (920 eV)/W (179 eV) or the Cu (920 eV)/Cu (60 eV) ratio with temperature are observed (figure 4.4 a). Copper neither dewets nor diffuses into the clean tungsten surface. These results are consistent with TDS data showing that Cu desorbs from W only above 1000 K (26).

For the Cu (1 ML)/$W_xN$/W interface, instability occurs above 550 K. In figure 4.4 b, the Cu (920 eV)/W (179 eV) ratio begins to decrease at 550 K and reaches a minimum at 750 K. In this same temperature range, the N Auger intensity increases (figure 4.5). Although changes in these values reflect variations in Cu surface concentration, they do not discriminate between Cu diffusion and three-dimensional Cu island formation at the surface. In figure 4.4 b (right axis) the Cu (920 eV)/Cu (60 eV) Auger intensity ratio increases from 550 to 750 K. As described above, this observation demonstrates copper diffusion into the nitride overlayer. From 750 to 900 K the Cu (920 eV)/W (179 eV) increases (figure 4.4 b), while the N Auger intensity decreases (figure 4.5). The decrease in N Auger signal corresponds to the mass 28 ($N_2$) leading edge signal (right y-axis) in the TDS spectrum (figure 4.5). This represents the initial decomposition of the nitride overlayer.

The increasing Cu (920 eV)/W (179 eV) ratio and decreasing Cu (920 eV)/Cu (60 eV) ratio represents increased exposure of the underlying diffused copper as the nitride decomposes. During the thermal decomposition of tungsten nitride, $N_2$ desorbs while the formerly nitrided tungsten diffuses back into the bulk tungsten. The observed higher

Cu(920 eV)/W (179 eV) ratio for 850 and 950 K after nitride decomposition compared to the Cu (920 eV)/W (179 eV) ratio before nitride decomposition, represents better wetting

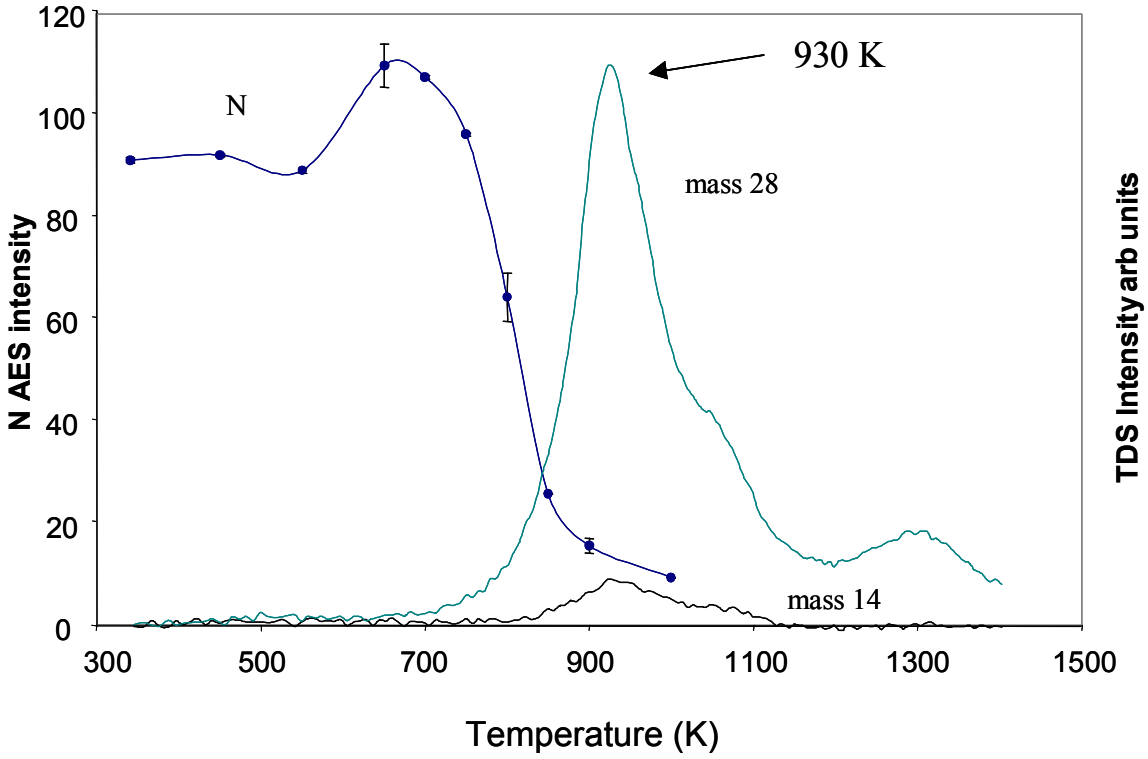


Figure 4.5. Nitrogen Auger intensity vs. temperature and thermal desorption spectroscopy for the Cu(1 ML)/$W_xN$/W system.

of Cu on the nitrogen free tungsten surface (figure 4.4 b). This is consistent with the observations in figure 4.2 where equivalent Cu deposition times results in higher Cu/W ratios for Cu on the clean tungsten surface compared to Cu on the nitrided surface.

## 4.4. Discussion

### 4.4.1. Cu Growth Behavior for Clean vs. Nitrided Tungsten

For copper on the clean tungsten surface, the characteristic ($i_A/i_S$) - t plot (figure. 4.2) indicates monolayer by monolayer or Frank Van der Merwe (FM) growth (15). Similar FM growth behavior has been reported previously for Cu on W (110) (26). The data presented here indicated similar growth behavior on polycrystalline vs. W (110) surfaces. The straight-line plots in the FM mode are observed due to a constant sticking probability. The distinctive breaks or changes in slope are due to succeeding layers attenuating a fraction of the substrate and adsorbate Auger emissions. The loss of part of the Auger emission is due to the inelastic scattering of the Auger electrons as they traverse the layer(s) (15). The FM mode can, in general, be explained by surface energy criteria formulated by Bauer (28). Wetting or FM growth is favored for the condition $\gamma_S > \gamma_A + \gamma_I$, where $\gamma_A$, $\gamma_I$ and $\gamma_S$ are the surface energies for the adsorbate, adsorbate-substrate interface and substrate, respectively. The effect of achieving local equilibrium or minimizing total surface energy is the completion of each copper layer. It is shown in figure 4.2 that the completion of the 1$^{st}$ copper monolayer (Cu/W atomic ratio ~ 1.1) is more rapid than that of the 2$^{nd}$ layer. The longer completion time for the 2$^{nd}$ layer is attributed to the decrease in sticking probability caused by a difference in heats of adsorption ($\Delta H_{ads}$) for copper on the tungsten surface versus copper on the 1$^{st}$ copper surface layer. The heat of adsorption is directly related to the residence time ($\tau$) of an atom or molecule on a surface by a two-dimensional phase approximation (29):

$$\tau = \tau_o \exp (\Delta H_{ads}/RT) \qquad (4.3)$$

In figure 4.3, a lower desorption temperature for copper sublimation (1140 – 1185 K, $t_{dep} > 4$ min.) is observed compared to copper desorbing from the tungsten (1220 K, $t_{dep} \leq 4$ min.). This demonstrates a lower activation energy to desorption for Cu bonded to the Cu atoms (bulk sublimation energy ~ 318 kJ/mol (30)), compared to Cu adsorbed on W (Redhead analysis desorption activation energy ~ 339 kJ/mol (31)). Since $\Delta H_{ads}$ is closely related to the activation energy of desorption (29), the residence time $\tau$ would be lower for copper layers above the 1st copper surface layer. The result of a lower residence time is the decrease in probability that a copper atom will be trapped in the surfaces attractive potential well. Thus longer deposition times will be needed to complete the second copper layer.

For copper deposited on the nitrided tungsten surface, the lack of changes or breaks in the slope for the $(i_A/i_S)$ - t plot (figure 4.2) is consistent with three-dimensional nucleation (non-wetting) or Volmer Weber (VW) growth. The VW mode follows the surface energy condition $\gamma_A + \gamma_I > \gamma_S$. The surface energy is minimized with the copper self-adsorbing as opposed to spreading over the tungsten surface. The straight line throughout the plot represents a constant sticking probability. The copper forms three-dimensional nuclei from the beginning of the deposition. The area between the three-dimensional nuclei reduces the probability that fractional attenuation of the Auger emissions will occur and that no changes in slope will be observed.

### 4.4.2. Thermal Induced Cu Diffusion and Instability of the Cu/Nitride/W Interface

Cu diffusion from the $W_xN$ surface to the $W_xN$/W interface is indicated by a decreasing Cu/W ratio and increasing Cu (920 eV)/Cu (60 eV) ratio from 550 – 750 K (section 3.2, figure 4.4 b. With increasing temperature, the Cu will preferentially migrate to form the strongest chemical interaction or increase in binding energy (29). Gomer et. al. reported the driving force for nitrogen segregation in an Cu/N/W(110) system (electron induced conversion of $N_2$ on W(110), N/W = 0.5) was an effect of Cu-N repulsion (32). Cu-N repulsion is not surprising considering that copper nitrides are known to be very unstable, with the standard heats of formation = +75 kJ/mol (33). In contrast, the interactions of Cu and W are very favorable where the enthalpy of adsorption = -371.1 kJ/mol (for Cu on W(110) (32). To understand the magnitude of the Cu-W interaction, the Cu Auger intensities before ($I_o$) and after (I) diffusion were used in equation (1) (section 2) to approximate the copper diffusion depth into the nitride overlayer. The estimated diffusion depth was ~ 10 Å, compared to an estimated nitride layer thickness of ~ 7.5 Å (section 2). The magnitude of the diffusion depth indicates that copper completely diffused through the nitride overlayer, which leads to interaction between Cu and W. Thus the driving force for Cu diffusion into the nitride overlayer is the effective Cu-nitride repulsion and more thermodynamically favorable Cu-W interaction.

As was shown for the TDS data in the figure 4.4, the nitride component of the Cu/$W_xN$/W system decomposes, resulting in the desorption of $N_2$ over the temperature range 750 – 1350 K. Compared to the $W_xN$/W system (i.e. no Cu), the leading edge for

$N_2$ desorption decreased by ~50 K (figure 4.1 vs. figure 4.4) and a significant decrease in the β-$N_2$ peak height (1350 K) was observed. Attard and King reported TDS measurements for various Cu coverages on $N_2$ predosed W (100) surfaces at room temperature (34) to examine the influence of co-deposited metal on N bonding. It was shown that with the addition of Cu, the leading edge displayed up to a 200 K decrease for $N_2$ desorption and a near complete removal of the β-$N_2$ peak (1350 K). Attard and King also commented on Ion Scattering Spectroscopy (ISS) measurements on the Cu/N/W(100) system where an observed decrease of the N ISS peak coincided with the Cu/W surface alloying temperature (~800 K) (35). In figure 4.4 from 800 – 900 K, the N AES signal attenuates sharply and falls on the inflection range of the $N_2$ desorption peak. These observations suggest that the addition of Cu weakens the W-N bonding (perturbs the N component) as the Cu-W alloy temperature is approached. The Cu-induced bond weakening is driven by the favorable Cu-W interaction (surface alloy) which effectively decreases the $N_2$ desorption for the Cu/$W_x$N/W system.

## 4.5. Summary and Conclusions

Auger electron spectroscopy and thermal desorption spectroscopy have been used to characterize the growth mode and thermal stability for Cu on clean and nitrided tungsten surfaces. Layer by layer (FM) growth occurs at 300 K for Cu on the clean tungsten surface, demonstrating a strong Cu-W interaction. Three- dimensional (VW) growth is observed for Cu on the nitrided tungsten surface, demonstrating a stronger Cu-Cu interaction than Cu-nitride interaction. For temperatures up to 1000 K, Cu (1 ML) is stable and neither dewets nor diffuses into the clean tungsten surface. At 550 K, Cu

begins diffusing into the 7.5-10 Å nitrided tungsten overlayer ($W_xN$/W). At 750 K, maximum diffusion of the Cu is observed. Above 750 K, the nitride overlayer decomposes, releasing $N_2$. A ~50 K decrease in leading edge $N_2$ desorption is observed for the Cu/$W_xN$/W compared to the $W_xN$/W.

The effective Cu-nitride repulsion drives the Cu to the more thermodynamically favorable tungsten region. The decrease in nitride decomposition temperature with the presence of Cu is due to perturbing effect of Cu on W-N bonding driven by a peculiar Cu-W surface alloy (~800 K) reported by Attard and King (35).

As device dimensions in ULSI continue to shrink, uniformity and conformity issues would be more problematic for Cu-$W_xN$ interfaces compared to Cu-tungsten interfaces. The strong room temperature interaction and thermal stability for Cu films $\leq$ 1 ML on W suggest ideal materials compatibility for monolayer sized interconnects (36). The poor Cu-nitride interaction and low diffusion temperature (550 K) suggest that tungsten nitrides may not be ideal as a diffusion barrier candidate at smaller device dimensions.

## 4.6. Chapter References

(1) Jain, A.; Ekstrom, B.; Adetutu, O. *Conference Proceedings ULSI XIV Materials Research Society*. **1999**, *14*, 305-311.

(2) Lu, J. P.; Hsu, W. Y.; Luttmer, J. D.; Magel, L. K.; Tsai, H. L. *J. Electrochem. Soc*. **1998**, *145 (2)*, L21.

(3) Kelsey, J.; Goldberg, C.; Nuesca, G.; Peterson, G.; Kaloyeros, A.; Arkles, B. *J. Vac. Sci. Technol. B*. **1999**, *17(3)*, 1101-1104.

(4) Uekubo, M.; Oku, T.; Nii, K.; Murakami, M.; Takahiro, K.; Yamaguchi, S.; Nakano, T.; Ohta, T. *Thin Solid Films*. **1996**, *286*, 170-175.

(5) Takeyama, M.; Noya, A. *Jpn. J. Appl. Phys*. **1997**, *36*, 2261-2266.

(6) Pokela, P. J.; Kwok, C. K.; Kolawa, E.; Raud, S.; Nicolet, M. A. *Applied Surf. Sci.* **1991**, *53*, 364-372.

(7) Suh, B.; Lee, Y.; Hwang, J.; Park, C. *Thin Solid Films*. **1999**, *348*, 299-303.

(8) Sun, S. C.; Tsai, M. H.; Chiu, H. T.; Chuang, S. H. *Symposium on VLSI Technology Digest of Technical Papers*. **1996**, 46-47.

(9) Park, B. L.; Ko, D. H.; Kim, Y. S.; Ha, J. M.; Park, Y. W.; Lee, S. I.; Lee, H. D.; Lee, M. B.; Chung, U. I.; Koh, Y. B.; Lee, M. Y. *Journal of Electronic Materials*. **1997**, *26 (2)*, L1-L5.

(10) Lin, J.; Tsukune, A.; Suzuki, T.; Yamada, M. *J. Vac. Sci. Technol. A*. **1999**, *17(3)*, 936-938.

(11) Vu, Q. T.; Pokela, P. J.; Garden, C. L.; Kolawa, E.; Raud, S.; Nicolet, M-A. *J. Appl. Phys.* **1990**, *68 (12)*, 6420-6423.

(12) Kattelus, H.; P., Kolawa, E.; Affolter, K.; Nicolet, M-A. *J. Vac. Sci. Technol. A*. **1985**, *3 (6)*, 2246-2254.

(13) Kasai, K.; Akasaka, Y.; Nakajima, K.; Suehiro, S.; Suguro, K.; Oyamatsu, H.; Kinugawa, M.; Kakumu, M. *International Electron Devices Meeting*. December 11-14, 1994, p. 497.

(14) Matsuhashi, H.; Nishikawa, S. *Jpn. J. Appl. Phys*. *Part 1*. **1994**, *33*, 1293.

(15) Argile, C.; Rhead, G. E. *Surface Science Reports: Adsorbed Layer and Thin Film Growth Modes Monitored by Auger Electron Spectroscopy;* Elsevier Science Publishers: B. V., North Holland, 1989; pp. 279-356.

(16) Chen, J. G.; Colaianni, M. L.; Weinberg, W. H.; Yates, Jr. J. T. *Surf. Sci.* **1992,** *279*, 223-232.

(17) Chen, J. G.; J. E. Crowell; Yates, Jr. J. T. *Surf. Sci.* **1987**, *185*, 373-393.

(18) Peden, C. H. F.; Kidd, K. B.; Shinn, N. D. *Journal of Vacuum Science and Technology A*. **1991**, *9 (3)*, 1518-1524.

(19) Murray, E.; Prasad, J.; Kelber, J. A. *Surf. Sci.* **1993**, *295,* L993.

(20) Davis, L. E.; MacDonald, N.C.; Palmberg, P. W.; Riach, G. E.; Weber, R. E. *Handbook of Auger Electron Spectroscopy*, *2nd ed.*; Physical Electronics: Eden Prairie, MN, 1976; pp. 1-12.

(21) Pend, Y. K.; Dawson, P. T. *Journal of Chemical Physics*. 1971, *54 (3)*, 950-961.

(22) Affolter, K.; Kattelus, H.; Nicolet, M.-A. *Mat. Res. Soc. Symp. Proc*. **1985**, *47*, 167.

(23) Feldman, L. C.; Mayer, J. W. *Fundamentals of Surface and Thin Film Analysis;* Prentice Hall: Englewood Cliffs, NJ, 1986; pp. 1-352.

(24) Powell, C. J. *Surf. Int. Anal.* **1995**, *23*, 121.

(25) Rhead, G. E.; Barthes, M. G.; Argile, C. *Thin Solid Films*. **1981**, *82*, 201.

(26) Bauer, E.; Poppa, H.; Todd, G.; Bonczek, F. *J. Appl. Phys*. **1974**, *45(12)*, 5167.

(27) Briggs, D.; Seah, M. P. *Practical Surface Analysis*; John Wiley & Sons Ltd: New York, 1983; pp. 1-533.

(28) Bauer, E.; Krist., Z. *Surface Sci.* **1958**, *110*, 372.

(29) Somerjai G. A. *Introduction to Surface Chemistry and Catalysis*; John Wiley & Sons, Inc.: NY, 1994; pp. 1-667.

(30) Kuhn, W. K.; Campbell, R. A.; Goodman, D. W. *J. Phys. Chem*. **1993**, *97*, 447.

(31) Redhead, P. A. *Vacuum*. **1962**, *12*, 205.

(32) Shamir, N.; Lin, J. C.; Gomer, R. *Surf. Sci*. **1989**, *214*, 74-84.

(33) Ozaki, A.; Aika, K. I. *A Treatise on Dinitrogen Fixation*; Hardy, R. W. F., Bottomley, F.; Burns, R. C.; Ed.; Wiley: New York, 1979; Chap. 4.

(34) Attard, G. A.; King, D. A. *Chem. Soc. Farady Trans*. **1990**, *86(15)*, 2735-2741.

(35) Attard, G. A.; King, D. A. *Surf. Sci*. **1989**, *188*, 589.

(36) Himpsel, F. J. *MRS Bulletin*. **1999**, *24 (8)*, 20-24.

REFERENCE LIST


Affolter, K.; Kattelus, H.; Nicolet, M.-A. *Mat. Res. Soc. Symp. Proc*. **1985**, *47*, 167.

Argile, C.; Rhead, G. E. *Surface Science Reports: Adsorbed Layer and Thin Film Growth Modes Monitored by Auger Electron Spectroscopy;* Elsevier Science Publishers: B. V., North Holland, 1989; pp. 279-356.

Attard, G. A.; King, D. A. *Chem. Soc. Farady Trans*. **1990**, *86(15)*, 2735-2741.

Attard, G. A.; King, D. A. *Surf. Sci*. **1989**, *188*, 589.

Azaroff, L. V. *Elements of X-ray Crystallography*; McGraw-Hill: New York, 1968; pp. 1-610.

Bauer, E.; Krist., Z. *Surface Sci.* **1958**, *110*, 372.

Bauer, E.; Poppa, H.; Todd, G.; Bonczek, F. *J. Appl. Phys*. **1974**, *45(12)*, 5167.

Bennighoven, A. *Secondary Ion Mass Spectrometry: Basic Concepts, Instrumental Aspects, Applications, and Trends*; J. Wiley: New York, 1987; pp. 1-1227.

Briggs, D.; Seah, M. P. *Practical Surface Analysis*; John Wiley & Sons Ltd: New York, 1983; pp. 1-533.

Carlson, T. A. *Photoelectron and Auger Spectroscopy*; Plenum Press: New York, 1975; pp. 1-417.

Chen, H.S.; Kimerling, L.C.; Poate, J.M.; Brown, W.L. *Appl. Phys. Lett.* **1978**, *32*, 461.

Chen, J. G.; Colaianni, M. L.; Weinberg, W. H.; Yates, Jr. J. T. *Surf. Sci.* **1992,** *279*, 223-232.

Chen, J. G.; J. E. Crowell; Yates, Jr. J. T. *Surf. Sci.* **1987**, *185*, 373-393.

Cohen, Samuel H. *Atomic Force Microscopy/Scanning Tunneling Microscopy*; Plenum Press: New York, 1994; pp. 1-453.

Cullity, B. D. *Elements of X-ray Diffraction*; Addison-Wesley: Reading, MA, 1956; pp. 1-514.

Davis, L. E.; MacDonald, N.C.; Palmberg, P. W.; Riach, G. E.; Weber, R. E. *Handbook of Auger Electron Spectroscopy*, *2nd ed.* Physical Electronics: Eden Prairie, MN, 1976; pp. 1-12.

de Jong, A. M., Niemantverdret, J. W. *Surf. Sci.* **1990**, *233*, 355.

Dror, S. *Scanning Force Microscopy: With Applications to Electric, Magnetic and Atomic Forces*; Oxford University Press: New York, NY, 1991; pp. 1-263.

Ebbing, Darrell D. *General Chemistry 2nd ed.;* Houghton Mifflin: Boston, MA, 1987, p. 790.

Ekerdt, J. G.; Sun, Y. M.; Szabo, A.; Szulczewski, G. J.; White, J. M. *Chemical Review.* **1996**, *96*, 1499-1517.

Feldman, L. C.; Mayer, J. W. *Fundamentals of Surface and Thin Film Analysis;* Prentice Hall: Englewood Cliffs, NJ, 1986; pp. 1-352.

Fryer, J. R. *The Chemical Applications of Transmission Electron Microscopy*; Academic Press: London; New York, 1979; pp. 1-286.

Gates, S. M. *Chemical Review*, **1996**, *96*, 1519-1532.

Goldstein, J. I.; Newbury, D. E.; Echlin, P.; Joy, D. C.; Fiori, C.' Lifshin, E. *Scanning Electron Microscopy and X-ray Microanalysis*; Plenum Press: New York, 1981; pp. 1-673.

Goldstein, J. I.; Yokowitz, H.; Newbury, D. E. *Practical Scanning Electron Microscopy: Electron and Ion Microprobe Analysis*; Plenum Press: New York, 1975; pp. 1-582.

Gray, W. D.; Loboda, M. J. *Solid State Technology*. March 2002, pp. 37-40.

Gupta, D.; Tu, K. N.; Asai, K. W. *Phys. Rev. Lett.* **1975**, *35*, 796.

Heidenreich, R. D. *Fundamentals of Transmission Electron Microscopy*; Interscience Publishers: New York, 1964; pp. 1-414.

Himpsel, F. J. *MRS Bulletin*. **1999**, *24 (8)*, 20-24.

Huntington, H. B. *Diffusion in Solids –Recent Developments*; Nowick, A. S. and Burton, J.J.; Eds.; Academic Press: New York, 1975; p. 303.

International Technology Roadmap of Semiconductors. 1999.

Jain, A.; Ekstrom, B.; Adetutu, O. *Conference Proceedings ULSI XIV Materials Research Society*. **1999**, *14*, 305-311.

Jeng, S.-P.; Havemann, R. H.; Chang, M.-C. *Mater. Res. Soc. Symp. Proc*. **1994**, *337*, 25.

Kasai, K.; Akasaka, Y.; Nakajima, K.; Suehiro, S.; Suguro, K.; Oyamatsu, H.; Kinugawa, M.; Kakumu, M. *International Electron Devices Meeting*. December 11-14, 1994, p. 497.

Kattelus, H.; P., Kolawa, E.; Affolter, K.; Nicolet, M-A. *J. Vac. Sci. Technol. A*. **1985**, *3 (6)*, 2246-2254.

Kelsey, J.; Goldberg, C.; Nuesca, G.; Peterson, G.; Kaloyeros, A.; Arkles, B. *J. Vac. Sci. Technol. B*. **1999**, *17(3)*, 1101-1104.

King, D. A. *Surf. Sci.* **1975**, *47*, 384.

Kolawa, E.; Pokela, P. J.; Reid, J. S.; Chen, J. S.; Ruiz, R. P.; Nicolet, M-A. *IEEE Electron Device Letters*. **1991**, *12 (6)*, 321.

Kubaschewski, O.; Evans, E. L.; Alcock, C. B. *Metallurgical Thermochemistry, 4th ed.*; Pergamon Press: Oxford, New York, 1967; pp. 1-495.

Kuhn, W. K.; Campbell, R. A.; Goodman, D. W. *J. Phys. Chem*. **1993**, *97*, 447.

Larrabee, G.B. *Materials Characterization for VLSI*; Einspruch, N. G.; Ed.; Academic Press: Orlando, FL, 1981; Vol. 2, p. 37.

Lin, J.; Tsukune, A.; Suzuki, T.; Yamada, M. *J. Vac. Sci. Technol. A*. **1999**, *17(3)*, 936-938.

Lu, J. P.; Hsu, W. Y.; Hong, Q. Z.; Dixit, G. A. *Advanced Metallization and Interconnect Systems for ULSI Applications in 1997*. Materials Research Society: Warrendale, PA, 1998; p. 87.

Lu, J. P.; Hsu, W. Y.; Luttmer, J. D.; Havemann, R. H. *Conference Proceedings ULSI XII Materials Research Society.* **1998**, 87-93.

Lu, J. P.; Hsu, W. Y.; Luttmer, J. D.; Magel, L. K.; Tsai, H. L. *Journal of the Electrochemical Society*. **1998**, *145 (2)*, L21-L22.

Lu, J. P.; Hsu, W. Y.; Luttmer, J. D.; Magel, L. K.; Tsai, H. L. *J. Electrochem. Soc*. **1998**, *145 (2)*, L21.

Marcus, R. B.; Sheng, T. T. *Transmission Electron Microscopy of Si VLSI Devices and Structures*; John Wiley & Sons, Inc.: New York, 1983; pp. 1-217.

Marcus, S. D.; Foster, R.F. *Thin Solid Films*. **1993**, *236*, 333.

Matsuhashi, H.; Nishikawa, S. *Jpn. J. Appl. Phys*. *Part 1*. **1994**, *33*, 1293.

McBrayer, J. D.; Swanson, R. M.; Sigmon, T. W. *Journal of the Electrochemical Society*. **1986**, *133*, 1243.

Milnes, A. G. *Deep Impurities in Semiconductors*; John Wiley & Sons: New York, 1973, pp. 1-526.

Mittal, K. L. *Vacuum Technology and Coating*. **2001**, *2 (12)*, 45-48.

Mori, H.; Imahori, J. Oku, T.; Murakami, M. *AIP Conference Proceedings*, **1998**, *418*, 475-480.

Muraka, S. P. *Metallization Theory and Practice for VLSI and ULSI*; Butterworth-Heinemann: Boston, MA, 1993; pp. 3-6, 70-74, 126-136, 142, 143, 172, 173, 228.

Murarka, S. P. Proc. *Int. Conf. Adv. Microelectronic Devices and Processing; Tohoku University: Sendai, Japan*, March 3 to 5, 1994, p. 321.

Murarka, Shyam P.; Hymes, Steven W. *Critical Reviews in Solid State and Materials Sciences*. **1995**, *20 (2)*, 87-124.

Murr, L. *Electron and Ion Microscopy and Microanalysis*; Marcel Dekker Inc: New York, 1982; pp. 1-793.

Murray, E.; Prasad, J.; Kelber, J. A. *Surf. Sci.* **1993**, *295,* L993.

Nakajima, T.; Watanabe, K.; Watanabe, N. *Journal of the Electrochemical Society*. **1996**, *134*, 3175.

Nguyen, T.; Charneski, L.; Hsu, S. T. *Journal of the Electrochemical Society*. **1997,** *144 (8)*, 2829-2833.

Ozaki, A.; Aika, K. I. *A Treatise on Dinitrogen Fixation*; Hardy, R. W. F., Bottomley, F.; Burns, R. C.; Ed.; Wiley: New York, 1979; Chap. 4.

Park, B. L.; Ko, D. H.; Kim, Y. S.; Ha, J. M.; Park, Y. W.; Lee, S. I.; Lee, H. D.; Lee, M. B.; Chung, U. I.; Koh, Y. B.; Lee, M. Y. *Journal of Electronic Materials*. **1997**, *26 (2)*, L1-L5.

Park, Lee M-B.; Moon, K-J.; Lee, H-D; Kang, H-K; Lee, M-Y. *Conference Proceedings ULSI XII Materials Research Society*. **1998**, 163-167.

Peden, C. H. F.; Kidd, K. B.; Shinn, N. D. *Journal of Vacuum Science and Technology A*. **1991**, *9 (3)*, 1518-1524.

Pend, Y. K.; Dawson, P. T. *Journal of Chemical Physics*. 1971, *54 (3)*, 950-961.

Peterson, N. L. *Diffusion in Solids - Recent Developments*; Nowick, A. S. and Burton, J. J.; Eds.; Academic Press: New York, 1975; p. 116.

Pokela, P. J.; Kwok, C. K.; Kolawa, E.; Raud, S.; Nicolet, M. A. *Applied Surf. Sci.* **1991**, *53*, 364-372.

Powell, C. J. *Surf. Int. Anal.* **1995**, *23*, 121.

Prometrix Auto RS55/tc manuel, # 04-0187 A, 1994, pp. A1 - A9.

Redhead, P. A. *Vacuum*. **1962**, *12*, 203-211.

Reid, J. S.; Sun, X.; Kolawa, E.; Nicolet, M. A. *IEEE Electron Device Letters.* **1994**, *15 (8)*, 298.

Rhead, G. E.; Barthes, M. G.; Argile, C. *Thin Solid Films*. **1981**, *82*, 201.

Rossnagel, S. M. *Materials Research Society.* **1995**, *354*, 503.

Saraswat, K. C.; Mohammadi, F. *IEEE, Trans. Electron. Dev*. **1982**, *29*, 645.

Seah, M. P.; Dench, W. A. *Surface Interface Analysis*, **1979**, *1*, 2.

Shamir, N.; Lin, J. C.; Gomer, R. *Surf. Sci*. **1989**, *214*, 74-84.

Shirley, G. G.; Blish, R. C. *Proceedings of the 25$^{th}$ Annual International Reliability Symposium, IEEE.* **1987**, 73.

Singer, P. *Semiconductor International*. February 1996, pp. 89-94.

Singer, P. *Semiconductor International*. **1997**, *20 (8)*, 79.

Singer, P. *Semiconductor International*. **1998**, *21 (6)*, 91-98.

Sinha, A. K.; Cooper, J. A. Jr.; Levinstein, H. H. *Electron. Dev. Lett*. **1982**, *3*, 90.

Siviram, S. *Chemical Vapor Deposition: Thermal and Plasma Deposition of Electronic Materials*; Van Nostrand Reinhold: New York, 1995; pp. 1-292.

Somerjai G. A. *Introduction to Surface Chemistry and Catalysis*; John Wiley & Sons, Inc.: NY, 1994; pp. 1-667.

Stolt, L.; d'Heurle, F.M.; Harper, J.M.E. *Thin Solid Films*. **1991**, *200*, 147.

Suh, B.; Lee, Y.; Hwang, J.; Park, C. *Thin Solid Films*. **1999**, *348*, 299-303.

Sun, S. C.; Tsai, M. H.; Chiu, H. T.; Chuang, S. H. *Symposium on VLSI Technology Digest of Technical Papers.* **1996**, 46-47.

Takeyama, M.; Noya, A. *Jpn. J. Appl. Phys*. **1997**, *36*, 2261-2266.

Tencor FLX-5200h manual # 274488 Rev. B, February, 1995, pp. 9-1 to 9-3.

The International Technology Roadmap For Semiconductors. 1999.

Thornton, P. R. *Scanning Electron Microscopy: Applications to Materials and Device Science*; Chapman and Hall: London, 1968; pp. 1-368.

Uekubo, M.; Oku, T.; Nii, K.; Murakami, M.; Takahiro, K.; Yamaguchi, S.; Nakano, T.; Ohta, T. *Thin Solid Films*. **1996**, *286*, 170-175.

Vazues, L.; Salvarezza, R. A.; Levy, R. A. *Applied Physical Letters*. **1996**, *68 (9)*, 1285-1287.

Vu, Q. T.; Pokela, P. J.; Garden, C. L.; Kolawa, E.; Raud, S.; Nicolet, M-A. *J. Appl. Phys.* **1990**, *68 (12)*, 6420-6423.

Walls, J. M. *Methods of Surface Analysis*; Cambridge University Press: New York, 1989; p. 223.

Wang, S-W. MRS Bulletin. August, 1994, p. 30.

Williams, P. *Analytical Chemistry*. **1977**, *49*, 1399.

Wittmer, M. *Journal of Vacuum Science and Technology A*. **1984**, *2(2)*, 273-280.

Wolf, S.; Tauber, R. N. *Silicon Processing for the VLSI Era, Volume 1 - Process Technology*; Lattice Press: Sunset Beach, CA, 1986; pp. 109-118, 161-197, 607, 608.

Wong, S. S.; Cho, J. S.; Kang, H.; Ryu, C. *Mat. Chem. & Phys.* **1995**, *41*, 229-233.